

①

1990

Thesis/Dissertation

Electron Density Comparisons Between Radar Observations  
and 3-D Ionospheric Model Calculations

Michael William Johnson

AFIT Student at: Utah State University

AFIT/CI/CIA - 90-109

AFIT/CI  
Wright-Patterson AFB OH 45433

Approved for Public Release IAW AFR 190-1  
Distribution Unlimited  
ERNEST A. HAYGOOD, 1st Lt, USAF  
Executive Officer, Civilian Institution Programs

DTIC  
ELECTE  
OCT 24 1990  
S B D  
E

AD-A227 703

Copyright © Michael William Johnson 1990  
All Rights Reserved

# ELECTRON DENSITY COMPARISONS BETWEEN RADAR OBSERVATIONS AND 3-D IONOSPHERIC MODEL CALCULATIONS

by

Michael William Johnson

A thesis submitted in partial fulfillment  
of the requirements for the degree

of

MASTER OF SCIENCE

in

Physics  
(Upper Atmospheric Option)

Accession For	
NTIS GRA&I	<input checked="" type="checkbox"/>
DTIC TAB	<input type="checkbox"/>
Unannounced	<input type="checkbox"/>
Justification	
By	
Distribution/	
Availability Codes	
Dist	Avail and/or Special
A-1	

Approved:

*Christ. Johnson*  
Major Professor

*Jan J. Sijka*  
Committee Member

*Lamorne E. Higgs*  
Committee Member

*Lamorne E. Higgs*  
Dean of Graduate Studies



UTAH STATE UNIVERSITY  
Logan, Utah

1990

# TABLE OF CONTENTS

	Page
ACKNOWLEDGEMENTS .....	ii
LIST OF TABLES .....	vii
LIST OF FIGURES .....	viii
LIST OF PLATES .....	ix
ABSTRACT .....	x
 I. INTRODUCTION .....	 1
II. LITERATURE REVIEW .....	4
2.1 Incoherent-Scatter Radar .....	4
2.1.1 Ionospheric Effects on Electromagnetic Radiation .....	4
2.1.2 Incoherent-Scatter Theory .....	6
2.1.3 Data Processing and Analysis of Incoherent-Scatter Data ...	14
2.1.4 Signal Processing .....	17
2.1.5 Radar Descriptions .....	18
2.2 USU-TDIM Model .....	21
2.2.1 General Description .....	21
2.2.2 Theoretical Development .....	22
2.2.2.1 Plasma diffusion .....	24
2.2.2.2 Photochemistry .....	26
2.2.2.3 Thermal structure .....	29
2.2.2.4 Model input parameters .....	30
2.3 Previous Studies .....	32
III. DATA PROCESSING .....	35
3.1 Temporal and Spatial Resolution .....	35

3.1.1 Radar Resolution . . . . .	35
3.1.2 Model Resolution . . . . .	36
3.2 Averaging Radar Data . . . . .	36
3.2.1 Processing Common to all Three Radars . . . . .	37
3.2.2 Sondrestrom Processing . . . . .	37
3.2.3 Millstone Processing . . . . .	39
3.2.4 Arecibo Processing . . . . .	39
3.3 Running the TDIM Model . . . . .	40
3.3.1 Description of the Model Runs . . . . .	40
3.3.2 Seasonal, Solar Cycle, and Geomagnetic Definitions . . . . .	41
IV. ANALYSIS OF DATA . . . . .	45
4.1 Plate 1, Comparison of 17-19 Jan 1984 . . . . .	47
4.1.1 Sondrestrom Comparison . . . . .	47
4.1.2 Millstone Comparison . . . . .	47
4.1.3 Arecibo Comparison . . . . .	47
4.2 Plate 2, Model Sensitivity to Kp - An Alternate Model Comparison of 17-19 Jan 1984 . . . . .	49
4.2.1 Sondrestrom Comparison . . . . .	49
4.2.2 Millstone Comparison . . . . .	49
4.2.3 Arecibo Comparison . . . . .	51
4.3 Plate 3, Model Sensitivity to F10.7 - Comparison of 26-28 Jun 1984 . . . . .	51
4.3.1 Sondrestrom Comparison . . . . .	51
4.3.2 Millstone Comparison . . . . .	53
4.4 Plate 4, Comparison of 19-21 Sep 1984 . . . . .	53
4.4.1 Sondrestrom Comparison . . . . .	55
4.4.2 Millstone Comparison . . . . .	55
4.4.3 Arecibo Comparison . . . . .	55
4.5 Plate 5, 15-18 Jan 1985 . . . . .	56

4.5.1 Sondrestrom Comparison .....	56
4.5.2 Millstone Comparison .....	56
4.5.3 Arecibo Comparison .....	58
4.6 Plate 6, 19-22 Mar 1985 .....	58
4.6.1 Sondrestrom Comparison .....	58
4.6.2 Millstone Comparison .....	60
4.6.3 Arecibo Comparison .....	60
4.7 Plate 7, 14-17 Jan 1986 .....	61
4.7.1 Sondrestrom Comparison .....	61
4.7.2 Millstone Comparison .....	61
4.7.3 Arecibo Comparison .....	63
4.8 Plate 8, 23-26 Sep 1986 .....	63
4.8.1 Sondrestrom Comparison .....	65
4.8.2 Millstone Comparison .....	65
4.8.3 Arecibo Comparison .....	66
4.9 Plate 9, 1-5 Jun 1987 .....	66
4.9.1 Sondrestrom Comparison .....	66
4.9.2 Millstone Comparison .....	66
4.9.3 Arecibo Comparison .....	68
4.10 Plate 10, 12-16 Jan 1988 .....	69
4.10.1 Sondrestrom Comparison .....	69
4.10.2 Millstone Comparison .....	69
4.10.3 Arecibo Comparison .....	71
4.11 Plate 11-12, Comparison of Spring and Fall Equinox .....	71
4.12 Plate 13, Secondary Evening Peak at Millstone .....	74
4.13 Plate 14-16, High-Latitude Winter and Summer Cases with Geomagnetic Activity .....	74
4.14 Plate 17, Solar-Cycle Variation .....	79
4.15 Plate 18, Seasonal Variation .....	79
4.16 Plate 19, Daytime NmF2 Differences at Arecibo .....	82
V. DISCUSSION AND CONCLUSIONS .....	84

5.1 Summary of Major Trends Found .....	84
5.1.1 Overall Agreement Between the Model and Observations ..	85
5.1.2 Secondary Evening Peak at Millstone .....	86
5.1.3 Spring-Fall Equinox Differences .....	88
5.1.4 Tidal Structure at Arecibo .....	89
5.1.5 Daytime NmF2 Differences .....	90
5.1.6 Other Possible Trends .....	91
5.2 Conclusions .....	92
5.3 Recommendations for Future Study .....	92
REFERENCES .....	95

## LIST OF TABLES

Table	Page
1. Radar Descriptions . . . . .	20
2. Ion Chemistry and Reaction Rates . . . . .	28
3. Criticality of USU-TDIM Inputs . . . . .	31
4. Observed Solar and Geomagnetic Data . . . . .	43



## LIST OF FIGURES

Figure	Page
1. $\alpha^2$ variation of the power spectra . . . . .	9
2. $T_i$ variation of the power spectra . . . . .	11
3. $T_r$ ( $T_e/T_i$ ) variation of the power spectra . . . . .	12
4. Composition variation of the power spectra . . . . .	13
5. Relationship of the fluctuation spectrum in the ionosphere to the measured spectrum . . . . .	19
6. Typical azimuthal pattern used for a fixed position Sondrestrom scan . . . . .	38

## LIST OF PLATES

Plate	Page
1. Comparison of 17-19 Jan 1984 . . . . .	48
2. Model sensitivity to Kp - an alternate model comparison of 17-19 Jan 1984 . . . . .	50
3. Model sensitivity to F10.7 - comparison of 26-28 Jun 1984 . . . . .	52
4. Comparison of 19-21 Sep 1984 . . . . .	54
5. 15-18 Jan 1985 . . . . .	57
6. 19-22 Mar 1985 . . . . .	59
7. 14-17 Jan 1986 . . . . .	62
8. 23-26 Sep 1986 . . . . .	64
9. 1-5 Jun 1987 . . . . .	67
10. 12-16 Jan 1988 . . . . .	70
11. Comparison of spring and fall equinox #1 . . . . .	72
12. Comparison of spring and fall equinox #2 . . . . .	73
13. Secondary evening peak at Millstone . . . . .	75
14. High-latitude winter case with geomagnetic activity #1 . . . . .	76
15. High-latitude winter case with geomagnetic activity #2 . . . . .	77
16. High-latitude summer case with geomagnetic activity . . . . .	78
17. Solar-cycle variation . . . . .	80
18. Seasonal variation . . . . .	81
19. Daytime NmF2 differences at Arecibo . . . . .	83

## ABSTRACT

### Electron Density Comparisons Between Radar Observations and 3-D Ionospheric Model Calculations

by

Michael W. Johnson, Master of Science

Utah State University, 1990

Major Professor: Dr. Vincent B. Wickwar  
Department: Physics (Upper Atmospheric Option)

For the first time, a comparison of electron densities calculated from the Utah State University First-Principals Ionospheric Model with simultaneous observations taken at Sondrestrom, Millstone, and Arecibo incoherent-scatter radars was undertaken to better understand the response of the ionosphere at these longitudinally similar yet latitudinally separated locations. The comparison included over 50 days distributed over 3 1/2 years roughly symmetrical about the last solar-minimum in 1986. The overall trend of the comparison was that to first-order the model reproduces electron densities responding to diurnal, seasonal, geomagnetic, and solar-cycle variations for all three radars. However, some model-observation discrepancies were found. These include, failure of the model

to correctly produce an evening peak at Millstone, fall-spring equinox differences at Sondrestrom, tidal structure at Arecibo, and daytime NmF2 values at Arecibo.

*...; ...; ...;*  
~~(110 pages)~~

# CHAPTER I

## INTRODUCTION

Over the last twenty years our knowledge of the ionosphere has grown tremendously. This has occurred largely because of an increased observational capability which has led to the evolution of ionospheric theories, empirical models, and finally, physical models.

One of the primary observational instruments is incoherent-scatter radar (ISR). This radar is capable of measuring nearly all ionospheric parameters and can make observations throughout the ionospheric altitude range. Unfortunately, because of its cost, only a few have been built, and those are strategically located so as to maximize their scientific usefulness.

Probably the most complete physical model to date is the Utah State University Time Dependent Ionospheric Model (USU-TDIM), developed by *Schunk* and co-workers [*Sojka*, 1989]. As the name implies it is a time-stepping numerical model which rigorously calculates ionospheric parameters over the globe (see model description in Chapter II). A natural step in the continuing development of the TDIM is to compare predicted values with observations. In this way, the ability of the model to reproduce observed parameters can be tested, and better insight can be gained as to what aspects of the ionosphere we understand well and what aspects we do not.

This study compares coordinated incoherent-scatter-radar observations of ionospheric density with those predicted by the TDIM. The radars used are Arecibo, Millstone Hill, and Sondrestrom. These lie approximately on the same longitude and provide good latitudinal coverage of the northern hemisphere. The latitudinal regimes of the ionosphere

covered include high latitude (Sondrestrom), mid latitude (Millstone Hill), and low mid latitude (Arecibo). The time interval covered includes 17 "World-Day" periods from 1984 through 1988. World days are days on which several incoherent-scatter radars and other instruments, in a coordinated effort, make observations over the same time interval. These coordinated observations typically run 2-3 days and are often scheduled as close to winter solstice, summer solstice, spring equinox, or fall equinox as possible. The data for this study were obtained from the incoherent-scatter database NCAR.

The earth's ionosphere exhibits significant variations with respect to altitude, latitude, longitude, universal time, solar cycle, season, and geomagnetic activity. This study should particularly emphasize diurnal altitude variations, seasonal variations, and latitudinal variations. Excellent reviews summarizing these differences and ionospheric theory in general can be found in *Schunk* [1983], *Nagy and Schunk* [1987], and *Rishbeth* [1988].

Past efforts have focussed on comparisons between ionosonde observations and model outputs of peak electron density of the F2 layer ( $N_mF2$ ) and the height of that peak density ( $H_mF2$ ) at mid and low latitudes or on high-latitude model-radar comparisons using one or two radars and covering one or two days (see review of past studies in Chapter II). These previous model-radar studies identified differences in the comparison, however, it was not evident that these differences were systematic. In other words, did they persist day after day or were they unique to the short period of the study? This study identifies systematic differences, it is the next logical step to previous model-radar comparisons of shorter duration. It extends those comparisons to three radars and to

many days. Therefore, it tests the model calculations much more severely. With one radar it is relatively easy to adjust input parameters to obtain agreement. As more radars are included, full density profiles used, and many days compared, the systematic agreements or disagreements between model calculations and observations become more meaningful.

The objective here is to emphasize major trends in the comparisons rather than trying to match input parameters to specific days and comparing fine-scale structure for those days. By major trends I mean primarily the similarities and differences between NmF2, HmF2, and the time variation of those parameters. However, one of the benefits of using incoherent-scatter radar data is the detail of electron density above and below HmF2; these features will also be examined.

## CHAPTER II

### LITERATURE REVIEW

#### 2.1 Incoherent-Scatter Radar

##### *2.1.1 Ionospheric Effects on Electromagnetic Radiation*

Experiments carried out during the first half of this century showed that a radio signal can be reflected by the ionosphere [Appelton and Barnett, 1926; Breit and Tuve, 1925]. This reflection will occur at an altitude where the radio frequency ( $f$ ) is equal to the plasma frequency ( $f_n$ ) [Ratcliffe, 1959]. The plasma frequency is given as

$$f_n = \frac{1}{2\pi} \left[ \frac{Ne^2}{m_e \epsilon_0} \right]^{1/2} \quad (2.1)$$

or  $f_n = 8.97 \times 10^6 N^{1/2}$  (Mhz), where  $N$  = electron density ( $1/m^3$ ),  $e$  = electron charge (C),  $m_e$  = electron mass (kg), and  $\epsilon_0$  = permittivity of free space (f/m). For typical ionospheric values of  $N$  ranging from  $10^{10}$  -  $10^{12}$  ( $1/m^3$ ),  $f_n$  will range from 1 - 10 MHz.

Early theory predicted that for radio waves with  $f \gg f_n$  there would be no reflection; this turns out to be true to the first and second order only. Very early on, J.J. Thomson (as described in Evans [1969]) demonstrated in the laboratory that individual electrons are capable of weakly scattering electromagnetic waves. In the case of backscattering, the cross section per electron is given by



$$\sigma_e = 4\pi r_e^2 \quad (2.2)$$

where  $\sigma_e$  = electron backscatter cross section, and  $r_e$  = electron radius [Evans, 1975]. It was hypothesized by Gordon that by illuminating a finite volume of the ionosphere with an electromagnetic wave, electrons, due to their random thermal motion, would scatter signals whose phases would be varying in time [Gordon, 1958]. Therefore, a receiver at the ground would simply need to add signal powers so that

$$\sigma = N\sigma_e \quad (2.3)$$

where  $\sigma$  = total radar cross section. Using the classical electron radius of  $2.8 \times 10^{-15}$  (m) and a representative electron density at the peak of the layer of  $10^{12}$  ( $1/\text{m}^3$ ) produces a radar cross section of only  $10^{-16}$  ( $\text{m}^2$ ). Thus, Gordon predicted that if a very high-powered beam of radio waves were used with a frequency well above the peak plasma frequency of the ionosphere ( $f_oF2$ ), an extremely small but still measurable amount of power would be backscattered. He calculated that a large antenna would need to be constructed to receive the low power signal scattered over a wide frequency range by the electrons.

The first experimental test of Gordon's predictions was performed by Bowles [1958]. It showed that Gordon's predictions were essentially correct except that the observed spectral width was considerably narrower than expected. Theoretical work using several different approaches has since shown that the influence of ions is to narrow the spectral width [Evans, 1969]. It is this concentration of the return spectrum which renders the

earth's ionosphere open to investigation using apparatus of considerably lower sensitivity than envisioned by Gordon. This type of scattering has been given the name incoherent (or Thomson) scattering even though it is not strictly *incoherent* because the ions provide a degree of *coherence*.

### 2.1.2 Incoherent-Scatter Theory

The nature of radio-wave scattering depends on the relative size of the radar wavelength to a characteristic length called the Debye length (D), which is given by

$$D = \left[ \frac{\epsilon_0 K T_e}{4\pi N e^2} \right]^{1/2} \quad (2.4)$$

where K = Boltzmann's constant and  $T_e$  = electron temperature.

For scale size greater than D, the plasma is neutral and the electrons and ions act collectively. Thus, when the exploring wavelength ( $\lambda$ ) is less than the Debye length, the received spectrum is representative of the unperturbed motion of the electrons-- that predicted by Gordon; when the wavelength is greater than the Debye length, the spectral width is roughly that of using the mass of the ions but the velocity of the electrons [Hagfors, 1961]. Evans explains incoherent-scatter observations as originating from "density fluctuations brought about by longitudinal oscillations in the plasma-- the principal components will be waves introduced by the presence of the ions (ion-acoustic waves) and electron-induced waves at the plasma frequency and electron gyrofrequency" [Evans, 1969, p. 499.]

The theoretical power spectrum as a function of frequency,  $S(f)$ , has been derived in several different ways by a number of authors [*Dougherty and Farley*, 1960; *Salpeter*, 1960; *Hagfors*, 1961; and others]. I will not show the equation here. However, the individual terms of the equation can be grouped into an electronic component and an ionic component. In order to compare these two components to see which is dominant, the parameter ( $\alpha^2$ ) is useful. Where

$$\alpha^2 = \left[ \frac{4\pi D}{\lambda} \right]^2 \quad (2.5)$$

When  $\alpha \geq 10$ , the scattered energy is entirely due to the electronic component and has a Gaussian spectrum with a width proportional to the thermal speed of the electrons. For  $0.5 \leq \alpha \leq 2.0$ , the spectrum appears as the sum of the two components. When  $\alpha < 0.5$ , as  $\alpha \rightarrow 0$  the amount of power in the electronic component decreases and appears as two lines displaced from the transmitted frequency by approximately the plasma frequency [*Evans*, 1969]. For data sets used in this work,  $\alpha^2$  ranges from 0 to a little less than 1. The Doppler width is given by

$$\Delta f_i = \frac{1}{\lambda} \left[ \frac{8KT_i}{m_i} \right]^{1/2} \quad (2.6)$$

where  $\Delta f_i$  = Doppler width of the ion component,  $T_i$  = ion temperature, and  $m_i$  = ion mass.

The total radar cross section, originally given by (2.3), is modified for the ionic

component so that when  $T_e = T_i$ ,

$$\sigma = \frac{\sigma_e}{(1+\alpha^2)(2+\alpha^2)} \quad (2.7)$$

or when  $T_e \neq T_i$ ,

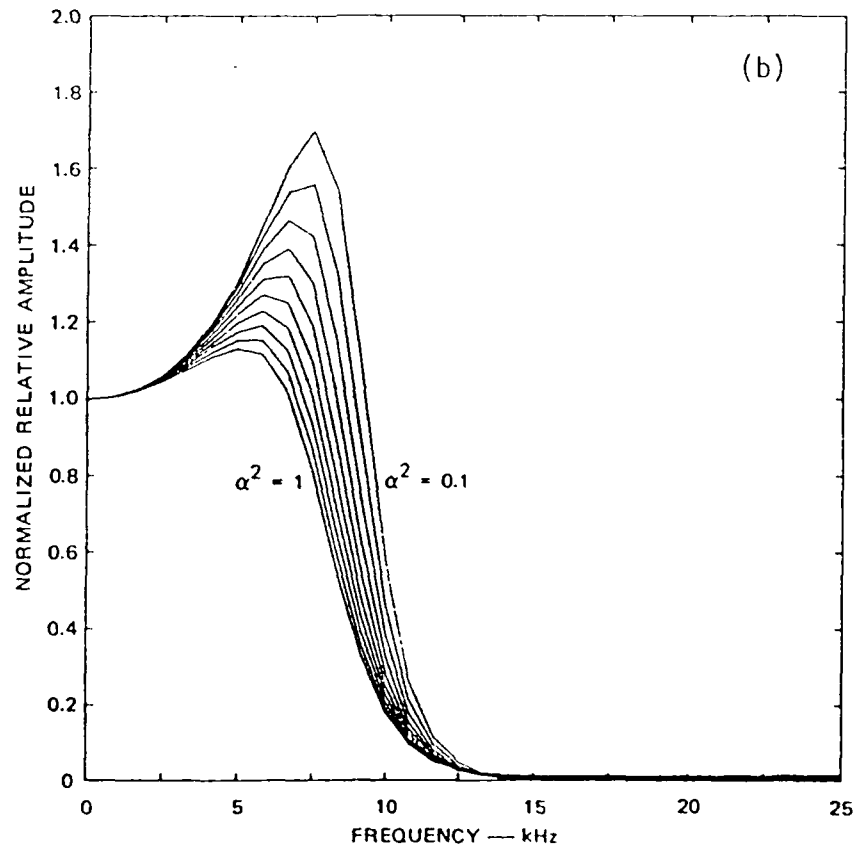
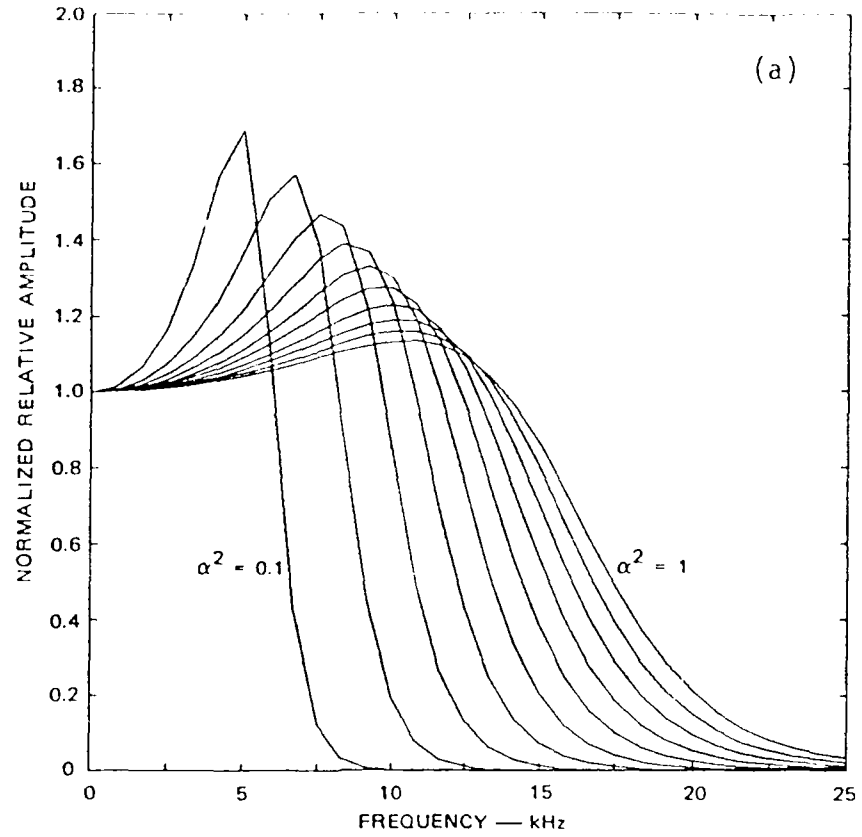
$$\sigma = \frac{\sigma_e}{(1+\alpha^2)(1+T_e/T_i+\alpha^2)} \quad (2.8)$$

[Moorcroft, 1963]. Equation (2.8) is only valid for a small range of  $T_e/T_i$ . Fortunately, for the range of  $T_e/T_i$  encountered in the ionosphere (2.8) does not introduce serious error [Evans, 1969].

There are three important aspects of the returned spectrum. First, the power (area under the spectrum) is proportional to the electron density. Second, the Doppler shift of the spectrum is proportional to the line-of-sight ion velocity. Third, the detailed shape of the spectrum provides information on electron and ion temperatures. At higher altitudes where  $H^+$  is present, it provides information on the ion composition. At lower altitudes it provides information on ion-neutral collisions. There are five parameters that describe the spectral shape. A brief discussion of each follows.

a. The parameter  $\alpha^2$  -

As discussed previously,  $\alpha^2$  characterizes the degree to which the ions affect the returned spectra (see Figure 1).



b. The ratio  $T_e/T_i$  (or  $T_r$ ) -

This ratio (primarily  $T_i$ ) changes the width of the spectrum; see (2.6) and Figure 2. In addition,  $T_r$  affects the peak-to-valley ratio, see Figure 3.

c. Ionic composition -

For density calculations (those of concern in this study), the ion composition has almost no effect. However, temperature calculations are very dependent on ion composition effects. The Doppler width of the returned spectrum is proportional to the square root of the ionic mass, as can be seen from (2.6). The ionic mass must be guessed at or in some independent way determined. Fortunately,  $O^+$  is the major ionic component in most F-region cases. See Figure 4 for composition effects on the spectrum.

d. Magnetic fields -

If the wave propagation direction is normal to the lines of force and the exploring wavelength is on the order of the ion gyroradius, characteristic fluctuations will be imparted to the spectrum by the gyromotion of the ions. This effect has only been seen at the Jicamarca ISR in Peru (near the magnetic equator) and serves in general to increase the total echo power when  $T_r > 1$ .

e. Collisions -

The derivation of the power spectrum equation was made assuming a

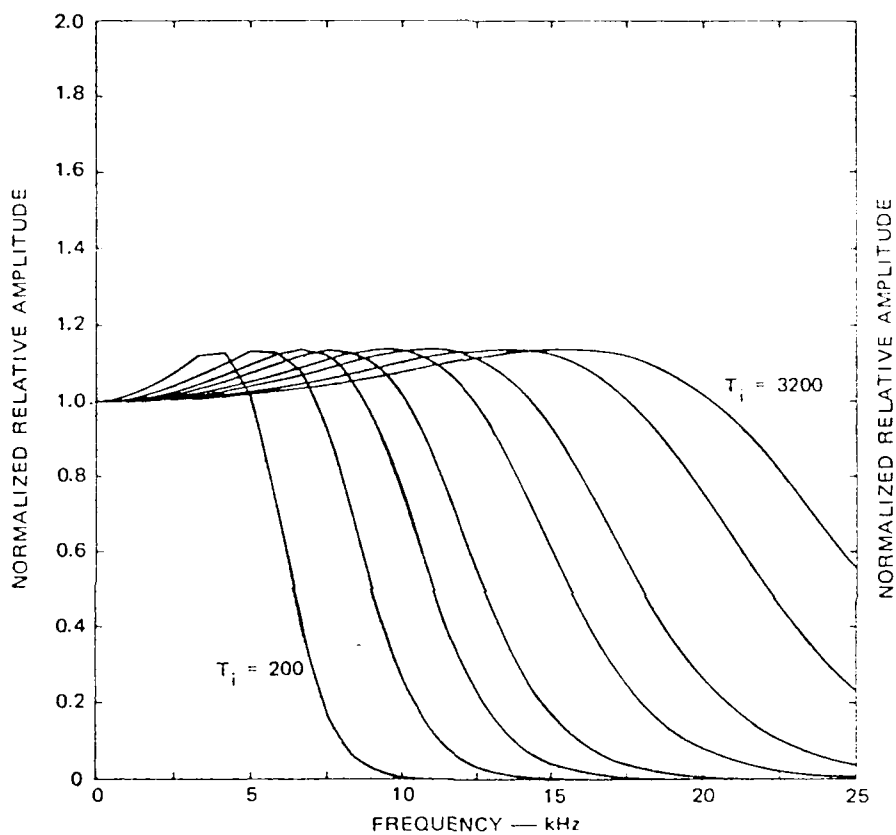


Fig. 2.  $T_i$  variation of the power spectra. The curves show eight values of  $T_i$  (200, 400, 600, 800, 1200, 1600, 2400, and 3200°K) for  $T_r = 1.0$ ,  $\alpha^2 \ll 1$ ,  $O^+$  composition, and a radar frequency of 1290 MHz. From Wickwar [1974].

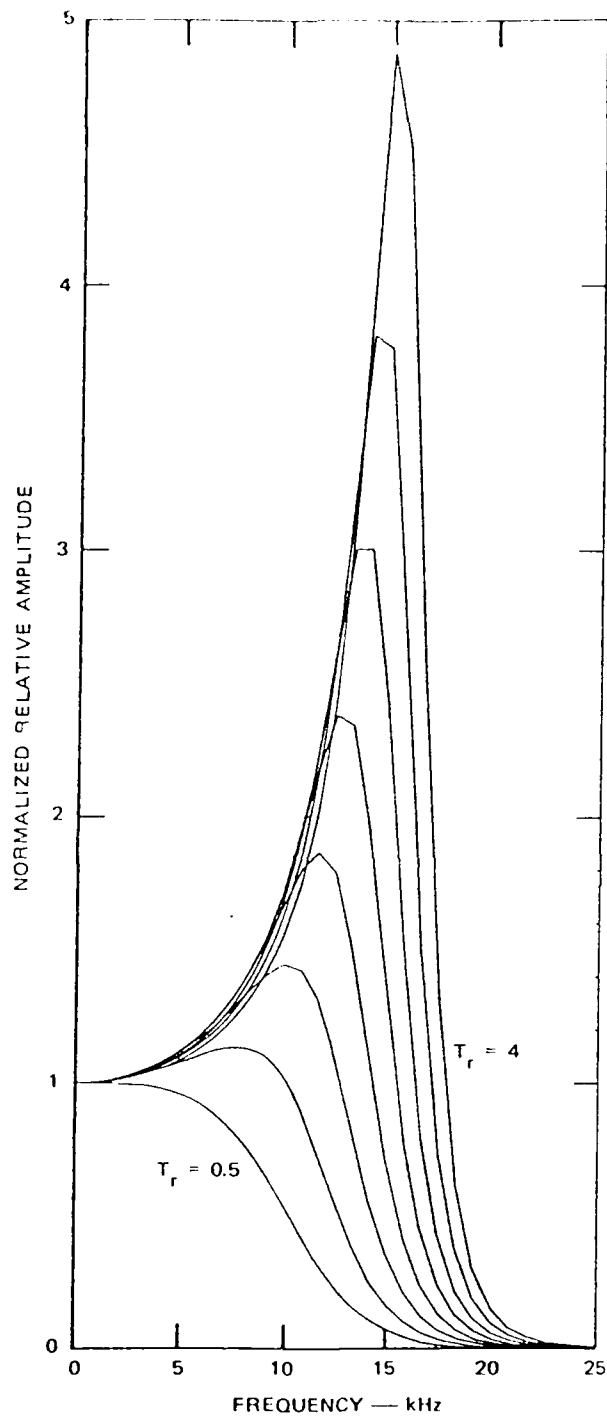


Fig. 3.  $T_r$  ( $T_r/T_i$ ) variation of the power spectra. Curve shows variations in  $T_r$  from 0.5 to 4.0 in steps of 0.5 for  $T_i = 800^\circ\text{K}$ ,  $\alpha^2 \ll 1$ , and  $\text{O}^+$  composition. These curves are similar to those in figure 2 and are also for a radar frequency of 1290 MHz. From Wickwar [1974].



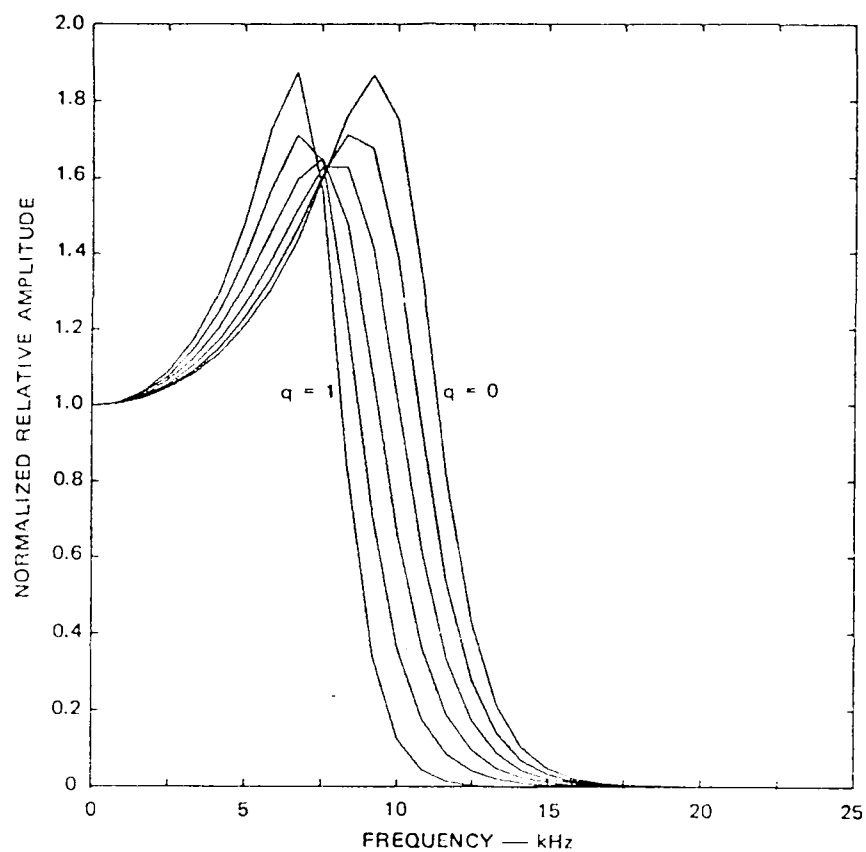


Fig. 4. Composition variation of the power spectra ( $q$ ), where  $q = N(O^+)/N(e)$ . The curve shows variation in composition from entirely mass 31 ions to entirely  $O^+$  ions (from  $q = 0.0$  to  $q = 1.0$  in steps of 0.2) for  $T_i = 500^\circ K$ ,  $T_e = 2.0$ , and  $\alpha^2 \ll 1$ . These curves are for a radar frequency of 1290 MHz. From Wickwar [1974].

collisionless plasma. It is therefore assumed that neutral collisions with ions are negligible when  $\lambda \gg 4\pi D$ . This is generally true when  $h > 120$  km and for wavelengths between 0.2 and 10 meters [Evans, 1969]. The main effect of collisions on the power spectrum is to make its shape more Gaussian; the total area under the curve is not greatly affected. Therefore, the derived temperature will change appreciably, but the deduced density is practically unaffected.

### *2.1.3 Data Processing and Analysis of Incoherent-Scatter Data*

There are several methods of calculating electron-density profiles with incoherent-scatter signals. One method is to examine the Faraday rotation of the backscattered wave [Evans, 1969]. Another is to measure the frequency offset of the plasma line [Yngvesson and Perkins, 1968]. However, the method used at Sondrestrom, Millstone Hill, and Arecibo is the one I alluded to earlier and involves the observation of the total returned power applicable to a particular height range. It takes into account temperature-dependent changes in the backscattering cross section, as discussed earlier.

In the previous section, the returned power spectrum was discussed as being a function of frequency  $S(f)$ . In actual practice, the signal is sampled in such a way as to produce an autocorrelation function (ACF), which is the Fourier transform of the power spectrum. So as to demonstrate an analysis technique, I will present an iterative method representative of Sondrestrom density calculations. This method was taken from Wickwar [1974] and V. B. Wickwar (personal communication, 1990). The actual method used at

a particular radar is hardware- and software-specific.

First, the radar equation is given by

$$P(r) = \frac{\kappa N(r) \sigma}{r^2} \quad (2.9)$$

where  $r$  = range,  $P(r)$  = returned power, and  $\kappa$  = proportionality constant which is radar dependent on the radar and its operating mode. Second,  $\sigma$ , as mentioned previously, is a function of  $T_r$  and of  $D$ . Therefore, a fictitious "raw density" ( $N'$ ) is derived from (2.9) by setting  $\alpha^2 = 0$  and  $T_r = 1$ . This equation is

$$N'(r) = \frac{P(r)r^2}{\kappa \sigma} \quad (2.10)$$

By using (2.8) and solving (2.9) for density in terms of (2.10) we get

$$N(r) = \frac{(1 + \alpha^2 + T_r)(1 + \alpha^2)}{2} N'(r) \quad (2.11)$$

Finally, to calculate  $N(r)$ ,  $\alpha^2$  and  $T_r$  must be known; the former is a function of both  $N$  and  $T_e$ .  $T_e$  and  $T_i$  (and thus  $T_r$ ) can be derived directly from the ACF. Since ACF information is available only at widely spaced intervals, a spline fit is done to interpolate between values. The real  $\alpha^2$  and  $N(r)$  can then be determined by the following iterative procedure:

- a. From (2.4) and (2.5),  $\alpha_j^2$  is given by

$$(\alpha_j)^2 = \left( \frac{4\pi\epsilon_0 K}{\lambda^2 e^2} \right) \frac{T_e}{N} \quad (2.12)$$

where the subscript (j) denotes an iterative quantity.

b. From (2.11),  $N_j$  becomes

$$N_j = \frac{(1 + \alpha_j^2 + T_e)(1 + \alpha_j^2)}{2} N' \quad (2.13)$$

c. Solve for  $\alpha_j^2$ ; next solve for  $N_j$ ; use the new  $N_j$  to solve for a new  $\alpha_j^2$  and so on.

Repeat this iteration until  $N_j$  varies by less than 1% from the previous value.

As mentioned before, the actual method used at a particular radar is software-dependent. A gist of the methods used at Sondrestrom, Millstone Hill, and Arecibo follows.

At Sondrestrom, the parameters are derived as described above. Normally a 48 km pulse length is used for all altitudes. However, sometimes the pulse length is varied with altitude. When it is, a 9 km pulse length is used for heights below 150 km and a 48 km pulse length is used for heights above 250 km; between 150 - 250 km, density calculations are made using 9 and 48 km pulse lengths which are then weighted by linear interpolation (V. B. Wickwar, personal communication, 1990).

At Millstone Hill, a least-squares fit of theoretical ACFs to the observed correlation functions is made to derive all parameters. Electron densities are then calculated by inserting a calibration constant into the radar equation (2.9). The constant used is

determined by comparing radar-derived electron densities from the F-region peak to  $f_0F_2$  ionosonde observations (converted to electron density). An effort is made to use high-elevation angle radar measurements and local ionosonde measurements. However, when overhead radar data do not exist, oblique radar data are used. The local ionogram sequence is shifted in local time to simulate density conditions at the oblique point of measurement (R. Musgrove, NCAR data header record, Feb. 4, 1985). For most radar experiments, ionospheric parameters are derived using 6, 30, 48, 96, 192, and 300 km pulse lengths. For this study, only the 96 km pulse length is used.

At Arecibo, the least squares fit of theoretical ACFs to the observed correlation functions is made to derive all parameters (V. B. Wickwar, personal communication, 1990). The calibration constant is determined by comparing the radar-derived electron densities from the peak of the F-layer to the peak electron density derived from ionosonde measurements. Prior to October 1985, the ACFs were determined using a 45 km long pulse with a new ACF determined every 22.5 km in range. Since then, a new 7-pulse scheme using 46.2 km long pulses has been used [Sulzer, 1986].

#### *2.1.4 Signal Processing*

As with any radar system, signal processing will alter the received waveform. With incoherent-scatter radars, two factors must be considered: a very low signal-to-noise ratio; and instrumental effects (transmitter, receiver, and digital processor).

Low signal-to-noise ratio is addressed by using relatively long integration times. This effectively limits the precision to which measurements can be made because of geophysical variations.

Instrumental effects distort the returned spectrum. These distortions are taken into account in the data reduction. The effects, as they apply to both frequency and time domains are summarized in Figure 5 [Baron *et al.*, 1970].

### 2.1.5 Radar Descriptions

A short description of the three radars used in this study follows (a summary of radar descriptions is given in Table 1).

Sondrestrom is located at Sondre Stromfjord, Greenland (67.0°N, 51.0°W), which is approximately 74° invariant latitude with a dip angle of 80°. The facility is operated by Stanford Research Institute (SRI) International. The radar is a pulsed system that transmits at 1290 MHz with a 60-320  $\mu$ s pulse length at a peak power of 4 MW. The antenna is a 32 m fully steerable Cassegrain dish. For further details see Kelly [1983] and Wickwar *et al.* [1984]. The receiver system is described in Kofman and Wickwar [1980].

Millstone Hill is located in Westford, Massachusetts (42.6°N, 71.5°W), which is approximately 53° invariant latitude with a dip angle of 72°. The facility is part of the Haystack Observatory operated by the Massachusetts Institute of Technology. The radar has two antennas, one fixed 67 m, and one fully steerable 46 m parabolic type. It also has two transmitters, they are pulsed systems with peak power of 2.5 MW each at a frequency of 440 MHz. They can be operated separately to each antenna or combined for 5 MW peak power. For further operational specifications see Evans *et al.* [1979].

The Arecibo radar is located near Arecibo, Puerto Rico (18.3°N, 66.8°W), which is approximately 32° invariant latitude with a dip angle of 49°. The facility is operated by

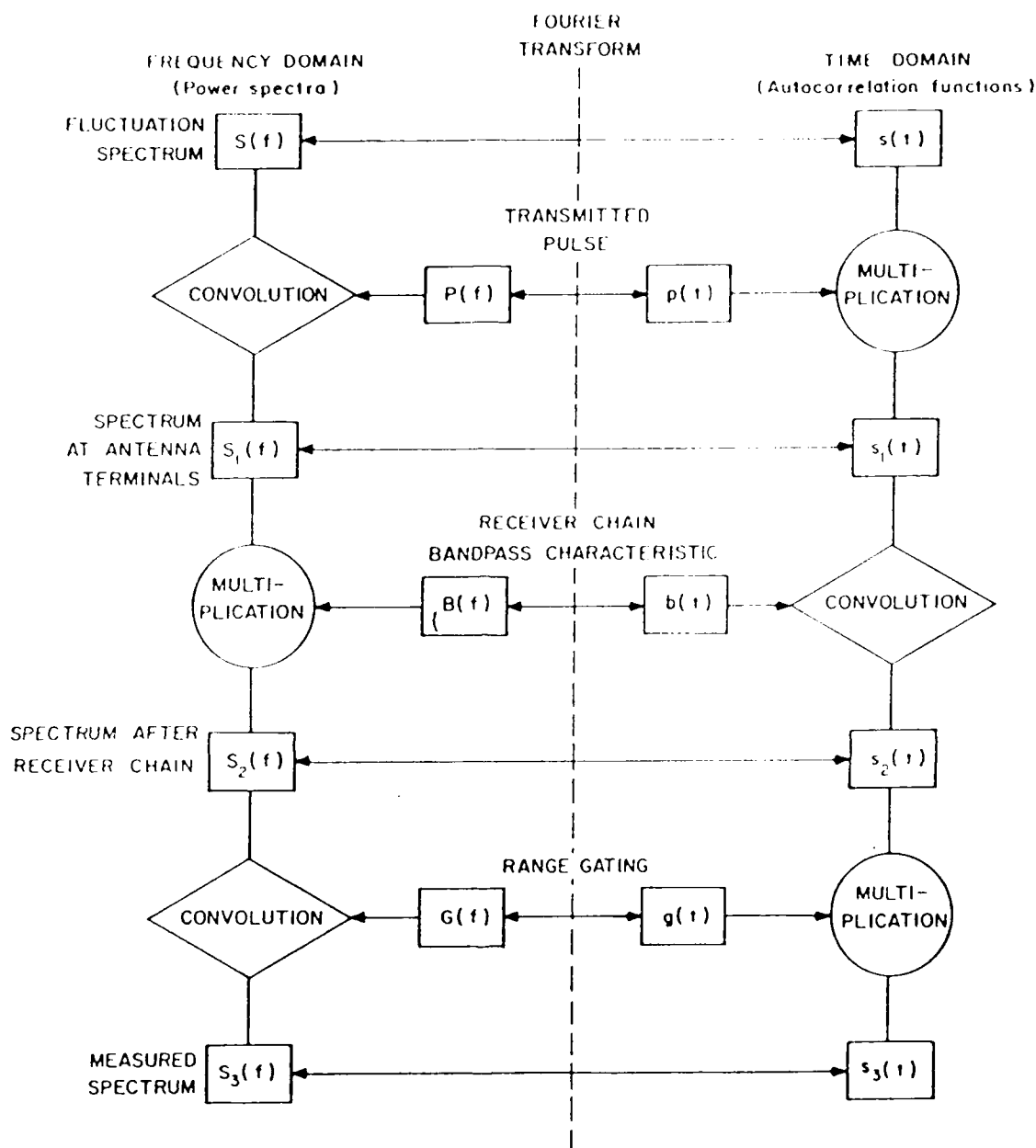


Fig. 5. Relationship of the fluctuation spectrum in the ionosphere to the measured spectrum. The signal is affected by the finite length of the transmitted pulse, the frequency response of the receiver, and the way in which the signal is sampled. The left-hand side shows how these factors enter in the frequency domain; the right-hand side shows how they enter in the time domain. From *Baron et al.* [1970].

TABLE 1. Radar Descriptions

## SONDRESTROM

>location: 67° N, 51° W (74° invariant latitude)

> dip angle: 80°

> specifications:  $f = 1290$  MHz

Peak Power = 4 MW

Pulse width = 60 - 320  $\mu$ s

## MILLSTONE HILL

>location: 43° N, 72° W (53° invariant latitude)

>dip angle: 72°

>specifications:  $f = 440$  MHz

Peak power = 2.5 MW (X 2)

Pulse width = 40 - 2000  $\mu$ s

## ARECIBO

>location: 18° N, 67° W (32° invariant latitude)

>dip angle: 49°

>specifications:  $f = 430$  MHz

Peak power = 2 - 2.5 MW

Pulse width ~ 320  $\mu$ s (seven pulse technique used after  
October 1985)



Cornell University. The radar is a pulsed system that transmits at 430 MHz with a peak power of 2-2.5 MW. A pulse width of 320 $\mu$ s is used, however the pulse technique was changed during the period of the data base used in this study. Before October 1985, a single long-pulse technique like that at Sondrestrom and Millstone Hill was used; after that time a 7-pulse technique using 7 long pulses was implemented [Sulzer, 1986]. The antenna is a fixed 300-m diameter spherical reflector constructed in a limestone sink hole. The line feed, positioned about 150 meters above the dish, can be moved so as to transmit and receive signals at angles up to 20° off zenith.

## 2.2 USU-TDIM Model

### 2.2.1 General Description

The Utah State University, Time Dependent Ionospheric Model (TDIM) has been developed over a fifteen-year period and has undergone several improvements [Schunk, 1988]. At the present time, the TDIM is a comprehensive, completely global, ionospheric first-principles model. It produces time-dependent three-dimensional distributions for ion and electron temperatures and densities. The model takes account of field-aligned diffusion, cross-field electrodynamic drifts, thermospheric winds, polar wind escape, energy-dependent chemical reactions, neutral composition changes, ion production due to solar EUV radiation and auroral precipitation, ion thermal conduction, ion diffusion-thermal heat flow, and local heating and cooling processes. It also allows for the offset between geomagnetic and geographic poles (UT effects).

### 2.2.2 Theoretical Development

In order to quantify the physical processes of the ionosphere, the TDIM solves a system of equations generally known as the transport equations. The three lowest order transport equations are the continuity, momentum, and energy equations, respectively.

These three equations expressed in a Lagrangian system and in CGS units are

$$\frac{\partial n_s}{\partial t} + \nabla \cdot (n_s \mathbf{u}_s) = P'_s - L'_s n_s \quad (2.14)$$

$$n_s m_s \left( \frac{D_s \mathbf{u}_s}{Dt} \right) + \nabla p_s + \nabla \cdot \boldsymbol{\tau}_s - n_s m_s \mathbf{G} - n_s e_s \left[ \mathbf{E} + \left( \frac{1}{c} \right) \mathbf{u}_s \times \mathbf{B} \right] = \frac{\delta M_s}{\delta t} \quad (2.15)$$

$$\left( \frac{D_s}{Dt} \right) \left( \frac{3}{2} \right) p_s + \left( \frac{5}{2} \right) p_s (\nabla \cdot \mathbf{u}_s) + \nabla \cdot \mathbf{q}_s + \boldsymbol{\tau}_s : \nabla \mathbf{u}_s = \frac{\delta E_s}{\delta t} + Q_s - L_s \quad (2.16)$$

where  $D_s/Dt = \partial/\partial t + \mathbf{u}_s \cdot \nabla$  is the convective derivative of species  $s$ ,  $p_s = n_s k T_s$  is the partial pressure,  $n_s$  is the number density,  $m_s$  is the mass,  $e_s$  is the charge,  $T_s$  is the temperature,  $\mathbf{u}_s$  is the drift velocity,  $\mathbf{q}_s$  is the heat flow vector,  $\boldsymbol{\tau}_s$  is the stress tensor,  $P'_s$  is the ionization production rate,  $L'_s$  is the ionization loss frequency,  $Q_s$  is the heating rate,  $L_s$  is the cooling rate,  $\mathbf{G}$  is the acceleration due to gravity,  $\mathbf{E}$  is the electric field,  $\mathbf{B}$  is the magnetic field,  $\partial/\partial t$  is the local time derivative,  $\nabla$  is the dell operator,  $c$  is the speed of light, and  $k$  is Boltzmann's constant. The double-dot operator in (2.16) corresponds to the scalar product of the two tensors. The quantities  $\delta M_s/\delta t$  and  $\delta E_s/\delta t$

represent the rate of momentum and energy exchange, respectively, between species  $s$  and the other species in the plasma [Schunk, 1988].

The momentum exchange term  $(\delta \mathbf{M}_s / \delta t)$  and energy exchange  $(\delta E_s / \delta t)$  of (2.15) and (2.16), are both functions of collision frequency and velocity distribution between neutral-ion-electron plasma species. The model assumes that collisions are random and velocity distribution can be represented by a displaced Maxwellian distribution such that

$$\frac{\delta \mathbf{M}_s}{\delta t} = \sum_t n_s m_s v_{st} (\mathbf{u}_t - \mathbf{u}_s) \quad (2.17)$$

$$\frac{\delta E_s}{\delta t} = n_s m_s \sum_t v_{st} \left[ 3k(T_t - T_s) + \frac{m_t (\mathbf{u}_s - \mathbf{u}_t)^2}{m_s + m_t} \right] \quad (2.18)$$

where the subscripts  $s$  and  $t$  denote the collision species, and  $v_{st}$  represents the intra-species ( $s$ - $t$ ) collisional frequency [Schunk, 1977, 1983]. Collision frequencies between charged species are both temperature and density dependent; and ion-neutral collisions are linearly proportional to the neutral density [Schunk, 1983]. Finally, it is noteworthy that  $v_{st} \neq v_{ts}$ , instead

$$n_s m_s v_{st} = n_t m_t v_{ts} \quad (2.19)$$

Before reviewing the general solution to the transport equations, I want to point out some of the physical processes which occur at different altitude regions of the ionosphere. Several of the assumptions made in the solution of the transport equations are based on distinguishing the dominant process occurring at different altitudes. There are three general ionospheric layers. First, there is a lower-ionospheric region (roughly 100-250 km) where photochemical processes dominate. Second, there is an upper-ionospheric region, where diffusion processes dominate (roughly 350-800 km). Third, there is a transition region where both processes have the same order of importance (250-350 km). Time constant arguments justifying this classification can be found in *Schunk* [1983].

*2.2.2.1 Plasma diffusion.* For plasma drifts perpendicular to the magnetic field, the momentum equation (2.15), is resolved into its perpendicular-drift components. The assumptions made include neglecting shear stress ( $\tau$ ), neglecting waves and assuming sub-sonic flow ( $D_s \mathbf{u}/Dt$ ), and neglecting horizontal momentum transfer ( $\delta \mathbf{M}_x / \delta t$ ). The resulting perpendicular drift equation becomes

$$\mathbf{u}_{\perp} = \frac{c(\mathbf{E} \times \mathbf{B})}{B^2} + \frac{mc}{eB^2}(\mathbf{G} \times \mathbf{B}) - \frac{c}{neB^2}(\nabla P \times \mathbf{B}) \quad (2.20)$$

where the subscript  $\perp$  denotes a component perpendicular to the magnetic field. The three terms listed on the right hand side of (2.20) are the electromagnetic, gravitational, and diamagnetic-plasma drifts, respectively. An additional assumption is made that the electromagnetic drift is the most dominant. Therefore, gravitational and diamagnetic drifts are neglected [*Schunk*, 1988]. The perpendicular plasma drifts are then

approximated by the electromagnetic drift only so that

$$\mathbf{u}_\perp \sim \mathbf{u}_E = \frac{c(\mathbf{E} \times \mathbf{B})}{B^2} \quad (2.21)$$

where the subscript E denotes electromagnetic drift.

For drifts parallel to the magnetic field, the model assumes ambipolar flow - (where ions and electrons move together, up or down field lines, like beads on a string) [Schunk, 1973]. The continuity equation (2.14) becomes

$$\frac{D_i n_i}{Dt} + \nabla_\parallel \cdot (n_i \mathbf{u}_{i\parallel}) = P_i - L_i n_i \quad (2.22)$$

where the subscript  $\parallel$  refers to a direction parallel to  $\mathbf{B}$ . The diffusion equation for major ions (and for the diffusion of electrons) is derived from (2.15) and is given by

$$\mathbf{u}_{i\parallel} = \mathbf{u}_{e\parallel} - D_i \left[ \frac{1}{n_i} \nabla_\parallel n_i + \frac{(\nabla \cdot \boldsymbol{\tau}_i)_\parallel}{n_i k T_i} - \frac{m_i G_\parallel}{k T_i} + \frac{1}{T_i} \nabla_\parallel (T_e + T_i) + \frac{(T_e / T_i)}{n_e} \nabla_\parallel n_e \right] \quad (2.23)$$

and

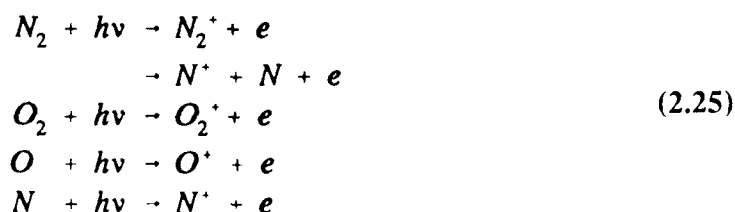
$$D_i = \frac{k T_i}{m_i \sum_n \nu_{in}} \quad (2.24)$$

Key assumptions made include assuming ambipolar flow ( $\mathbf{u}_i \sim \mathbf{u}_e$ ); assuming the polarization electrostatic field ( $\mathbf{E}_\perp$ ) is solely determined by the electrons (because of relative mobility between ions and electrons); neglecting waves and assuming sub-sonic flow ( $D_s \mathbf{u}/Dt$ ); and assuming the ion-neutral collision frequency ( $\nu_{in}$ ) is the dominant collision term in the momentum transfer equation ( $\delta \mathbf{M}_i/\delta t$ ).

The ambipolar-diffusion equation shown above (2.23) is solved for the major ions ( $O^+$ ,  $NO^+$ ,  $O_2^+$ ). In addition, the diffusion equation for the minor ions ( $He^+$ ,  $N_2^+$ ,  $N^+$ ) is solved. For a derivation of the latter equation see *Schunk* [1988].

I should stress that all of these equations are coupled. That is, for the six species of major and minor ions, an equation for each one is solved self-consistently as part of a system of equations.

**2.2.2.2 Photochemistry.** Ion and electron production and loss mechanisms include ionospheric photochemical reactions and production from auroral precipitation. Auroral precipitation is an input parameter to the model and is covered in the next section. For photochemical reactions, the TDIM reproduces the physical production and loss mechanisms believed to be occurring in the ionosphere. The most important of these include



the photoionization production rate is given by

$$P_e(E, z) = \sum_L \sum_n n_n(z) \int_0^\infty d\lambda I_\infty(\lambda) \sigma_n^{(0)}(\lambda) p_n(\lambda, E_L) \exp[-\tau(\lambda, z)] \quad (2.26)$$

and

$$\tau(\lambda, z) = \sum_n \sigma_n^{(a)}(\lambda) n_n H_n \text{ch}(R_n, \chi) \quad (2.27)$$

$$H_n = \frac{kT_n}{m_n g} \quad (2.28)$$

$$R_n = \frac{(R_e + z)}{H_n} \quad (2.29)$$

where  $P'_e$  is the photoelectron production rate;  $E = E_\lambda - E_L$ ,  $E_\lambda$  is the energy corresponding to wavelength  $\lambda$ ,  $E_L$  is the ionization energy of a given excited ion state (L);  $R$  is the planetary radius;  $\chi$  is the solar zenith angle;  $\text{ch}(R_n, \chi)$  is the Chapman grazing incidence function; and  $p_n(\lambda, E_L)$  are the branching ratios of the various excited ion states [Schunk, 1983]. Key assumptions include a solar radiation spectrum suggested by Torr *et al.* [1979] so that parameters dependent on wavelength ( $\lambda$ ) are varied and a constant neutral scale height ( $H_n$ ).

Chemical reactions included in the TDIM are shown in Table 2. The reaction rates

TABLE 2. Ion Chemistry and Reaction Rates, adapted from *Schunk* [1980].

28

Reaction	Rate Coefficients, $\text{cm}^3 \text{s}^{-1}$
$\text{O}^+ + \text{N}_2 \rightarrow \text{NO}^+ + \text{O}$	$k_1$
$\text{O}^+ + \text{O}_2 \rightarrow \text{O}_2^+ + \text{O}$	$k_2$
$\text{O}^+ + \text{NO} \rightarrow \text{NO}^+ + \text{O}$	$k_3$
$\text{O}_2^+ + \text{N}_2 \rightarrow \text{NO}^+ + \text{NO}$	$5 \times 10^{-16}$
$\text{O}_2^+ + \text{NO} \rightarrow \text{NO}^+ + \text{O}_2$	$4.4 \times 10^{-10}$
$\text{O}_2^+ + \text{N} \rightarrow \text{NO}^+ + \text{O}$	$1.2 \times 10^{-10}$
$\text{O}_2^+ + \text{e} \rightarrow \text{O} + \text{O}$	$1.6 \times 10^{-7} (300/T_e)^{0.55}$
$\text{N}_2^+ + \text{O} \rightarrow \text{NO}^+ + \text{N}$	$1.4 \times 10^{-10} (300/T)^{0.44}; T \leq 1500^\circ\text{K}$ $5.2 \times 10^{-11} (T/300)^{0.2}; T > 1500^\circ\text{K}$
$\text{N}_2^+ + \text{O} \rightarrow \text{O}^+ + \text{N}_2$	$1 \times 10^{-11} (300/T)^{0.23}; T \leq 1500^\circ\text{K}$ $3.6 \times 10^{-12} (T/300)^{0.41}; T > 1500^\circ\text{K}$
$\text{N}_2^+ + \text{O}_2 \rightarrow \text{O}_2^+ + \text{N}_2$	$5 \times 10^{-11} (300/T)$
$\text{N}_2^+ + \text{NO} \rightarrow \text{NO}^+ + \text{N}_2$	$3.3 \times 10^{-10}$
$\text{N}_2^+ + \text{e} \rightarrow \text{N} + \text{N}$	$1.8 \times 10^{-7} (300/T_e)^{0.39}$
$\text{NO}^+ + \text{e} \rightarrow \text{N} + \text{O}$	$4.2 \times 10^{-7} (300/T_e)^{0.85}$
$\text{He}^+ + \text{N}_2 \rightarrow \text{N}^+ + \text{N} + \text{He}$	$1 \times 10^{-9}$
$\text{N}^+ + \text{O}_2 \rightarrow \text{NO}^+ + \text{O}$	$2 \times 10^{-10}$
$\text{N}^+ + \text{O}_2 \rightarrow \text{O}_2^+ + \text{N}$	$4 \times 10^{-10}$
$\text{N}^+ + \text{NO} \rightarrow \text{NO}^+ + \text{N}$	$2 \times 10^{-11}$



for these reactions are temperature dependent and are given in *Schunk* [1983]. At mid latitudes, seasonal  $O^+(^2D)$  to  $N_2^+$  composition changes are incorporated as cited in *Schunk and references therein* [1988].

*2.2.2.3 Thermal structure.* Ion- and electron-temperatures gradients contribute to the pressure force which drives ambipolar flow (2.23). At lower altitudes, these temperatures effect chemical reaction rates. The TDIM calculates temperature profiles by solving the ion and electron energy equations.

The ion energy equation becomes

$$\nabla \cdot \mathbf{q}_i = \frac{\delta E_i}{\delta t} + Q_e - L_e \quad (2.30)$$

Key assumptions in this derivation include neglecting the convection term  $(D/Dt)(3/2)p_i$ , neglecting the advecting term  $[(5/2)p_i(\nabla \cdot \mathbf{u}_i)]$ , and neglecting the viscous-heating term  $(\tau_i : \nabla \mathbf{u}_i)$ . The ion heat flow of (2.30) is given by *Conrad and Schunk* [1979] as

$$\mathbf{q}_{i\parallel} = -K'_{ni} \nabla_{\parallel} T_i - K_{in} \nabla_{\parallel} T_n + R_{in} (\mathbf{u}_i - \mathbf{u}_n)_{\parallel} \quad (2.31)$$

where  $K'_{ni}$  and  $K_{in}$  are derived thermal conductivities and  $R_{in}$  is the diffusive-thermal coefficient. The main assumptions made in deriving (2.31) include assuming a collision-dominated partially-ionized plasma; assuming the ion heat flow is only relevant to high F-region altitudes and therefore using  $O^+$  and  $O$  as the dominant ion and neutral species, respectively; and assuming that the ion temperature ( $T_i$ ) can be represented by the major ion species only.

For the electrons, a temperature profile is generated using the electron continuity and electron energy equations. The electron energy equation becomes

$$\frac{3}{2}n_e k \frac{\partial T_e}{\partial t} = n_e k T_e (\nabla \cdot \mathbf{u}_e) - \frac{3}{2}n_e k u_e \cdot \nabla T_e - \nabla \cdot \mathbf{q}_e + \frac{\delta E}{\delta t} + Q_e - L_e \quad (2.32)$$

and

$$\mathbf{q}_{e\parallel} = -\beta_e J_{e\parallel} - K^e \nabla_{\parallel} T_e \quad (2.33)$$

where  $\beta_e$  is a thermoelectric coefficient and  $K^e$  is the electron thermal conductivity [Schunk, 1988]. Key assumptions include neglecting the viscous heating term ( $\tau_e : \nabla \mathbf{u}_e$ ) and neglecting production/loss mechanisms in the electron continuity equation (2.14).

Cooling rates for both elastic and inelastic collisions are calculated as shown in Schunk [1988]. Heating rate calculations are shown in Schunk [1983].

*2.2.2.4 Model input parameters.* The TDIM is a regional model, in other words, it reproduces physical processes at a specific region-- the ionosphere. However, this region is strongly coupled to the atmosphere below, the magnetosphere above, and to the neutral constituents within the ionosphere itself (thermosphere). Coupling mechanisms include electric fields, particle precipitation, field-aligned currents, heat flows, and frictional interactions. These coupled contributions must be input to the model and are either estimated as being negligible, or input as smoothed statistical averages. The most important input parameters are the adopted convection electric fields, auroral precipitation, thermospheric wind, composition, and electron heat flux, see Table 3.

TABLE 3. Criticality of USU-TDIM Inputs During (a) Quiet and (b) Disturbed Geomagnetic Activity, Adapted from *Sojka* [1989].

(a)			
Input Region	Zeroth Order	1st Order	Highest Order
Magnetosphere		Convection E Field	
Magnetosphere		Auroral Precipitation	Ion and Polar Cap Precipitation
Magnetosphere			Electron Heat Flux
Thermosphere		Wind	
Thermosphere			Density, Temperature
Thermosphere			Composition
Sun			Absolute EUV Spectrum
(b)			
Magnetosphere	Convection E Field	E Field Structure	
Magnetosphere	Auroral Precipitation	Arc Structure	
Magnetosphere		Electron Heat Flux	
Thermosphere		Wind	
Thermosphere		Composition	
Sun			Absolute EUV Spectrum

Adopted input parameters include thermospheric densities and temperatures from Mass Spectrometer and Incoherent Scatter (MSIS model) [Hedin, 1987]; an analytical expression for thermospheric wind pattern modified from *Murphy et al.* [1976]; an empirical plasma convection pattern, see for example *Sojka et al.* [1986]; and an empirical auroral oval, see for example *Feldstein and Starkov* [1967].

## 2.3 Previous Studies

A number of TDIM-observational studies have been conducted in the past ten years. Most of these have focussed on two areas: (a) limiting the time period of the study so that model input parameters could be closely matched to observed values and then testing model sensitivities or; (b) making comparisons using large observational data sets (such as ionosonde derived  $f_oF2$  and  $HmF2$ ) in order to study trends. A review of those comparisons most pertinent to this study follow.

*Murdin et al.* [1984] used incoherent-scatter radar data from Chatanika for both a geomagnetically-active and -quiet day in a comparison with derived TDIM electron densities. The study emphasized diurnal transport effects and highlighted the failure of the model to reproduce fine structure on the geomagnetically active day.

*Sojka et al.* [1983] compared plasma convection velocities and electron densities derived from Millstone Hill incoherent-scatter data with TDIM predicted values. A day near equinox with moderate magnetic activity was chosen for the comparison. Most of the observed features were reproduced by the model. Where differences did occur they were attributed to the auroral oval and convection electric field inputs to the model.

*Rasmussen et al.* [1986] compared TDIM electron-density predictions on two summer days with simultaneous radar observations from Chatanika and Millstone Hill. A great deal of effort was spent in adjusting empirical model inputs to the radar data and NOAA-6 satellite data whenever possible. The sensitivities of the four main model inputs, were closely scrutinized. Those inputs were the convection electric field, thermospheric winds, auroral-electron energy flux, and electron temperature distribution. Very good model-observation agreement was achieved, especially at Millstone Hill (50° invariant). However, some discrepancies were found at Chatanika (65° invariant) and the most likely cause was again attributed to model input limitations.

*Wilkinson et al.* [1987] compared ionosonde NmF2 and hmf2 for several sites with both the TDIM and the International Reference Ionosphere (IRI) empirical model. The period of study was near equinox using both geomagnetically-active and -quiet day. Model inputs for both the TDIM and IRI were initiated to predict average behavior. There was good agreement in most cases; however, there were phase differences and peak-density differences in the TDIM at low-latitude stations. These were attributed to the input low-latitude electric-field model, neutral-wind inputs, and the inability of the TDIM to reproduce gravity wave structure.

*Sojka et al.* [1988] used a localized yet very extensive observational data set for TDIM comparisons of complete diurnal, seasonal, and solar cycle trends for quiet geomagnetic conditions. He used ionosonde  $f_oF2$  data from the Argentine Islands' which had been processed by *Wrenn et al.* [1987] to represent quiet geomagnetic activity for yearly periods from solar-minimum to solar-maximum conditions. The Argentine Islands

ionosonde is a mid-latitude location ( $-58^\circ$  invariant). The TDIM by this time included rigorously calculated ion and electron temperatures, thus eliminating the need to use them as input parameters. However, this addition to the model created the need to input a solar flux spectrum. Diurnal trends were modeled successfully over all solar-cycle and seasonal conditions. Discrepancies that they found were attributed to the input solar spectrum flux, and neutral wind induced drifts. It was also noted that for this study, varying the MSIS atmosphere had little effect on  $f_0F2$ .

This present study is uniquely different from those just discussed. It combines the advantages of using highly detailed radar data (instead of ionosonde data which is limited to  $f_0F2$  and less reliable HmF2) and extending the comparison to many days, over several seasons so that systematic differences can be examined.

## CHAPTER III

# DATA PROCESSING

### 3.1 Temporal and Spatial Resolution

In order to make a meaningful comparison between radar- and model-derived electron-densities, consideration must be given to the temporal and spatial resolution of both. Generally speaking, the number of radar-density profiles available in a given time interval far exceeds the temporal resolution of the model. In addition, both model and radar need to give density profiles directly above each radar. Obviously, for temporal and spatial reasons, some averaging of the radar data must be performed before a comparison with the model can be made.

#### *3.1.1 Radar Resolution*

By averaging several radar observations together, a temporal and spatial mean-density profile was created. In the time domain, this should serve to smooth out some of the small-scale features in the radar observations that are unwanted in this comparison. Spatially, this averaged profile should represent the area directly above the radar. Factors leading to this conclusion follow. First, only high-elevation-angle data was selected. Second, in most cases the spatially averaged pattern was homogeneously spread around the radar. Third, large horizontal density gradients between averaged observations are not generally expected, this is especially true at Millstone and Arecibo. Vertical radar resolution has already been discussed in Chapter 2.

### *3.1.2 Model Resolution*

Model data generated for Sondrestrom and Millstone Hill was stored in the following manner. During every 24-hour period, 12 Universal Time (UT) bins were created. Each UT bin was then subdivided into 24 Magnetic Local Time (MLT) bins. This creates a temporal resolution for these runs of one hour of MLT, with a new MLT bin being created every other UT-hour. Twenty latitude bins were generated between 50°-90° (magnetic), this gives a 2° magnetic latitude resolution. For a given radar, if the horizontal area of the bin covered the geographic location of that radar, it was selected. In the vertical, there were 20 altitude bins ranging from 100 to 800 km. For the altitude range of this study (100-500 km), vertical-bin spacing ranged from 4 km (at 100 km altitude) to 22 km (at 500 km altitude).

At Arecibo, density bins were centered at its geographic location and stepped through 24 MLT hours. In other words, it was assumed that the ionosphere at this latitude co-rotates with the radar. Actually, the Millstone model data could also have been acceptably run in this manner. Vertical binning at Arecibo was done in the same way as at Millstone and Sondrestrom.

## **3.2 Averaging Radar Data**

All of the data received was on 9 track, 1600 bpi tapes which were archived in standard NCAR format. Data processing included: (a) reading the tapes onto the USU VAX8650 mainframe; (b) running data selection and averaging routines for each radar experiment while storing this processed data on a DECstation3100; (c) accessing these



files from a VAX1170 with a plotting routine; and (d) photographing the plots through an AED system to produce 3×5" color prints of the processed data (see Acknowledgements).

### *3.2.1 Processing Common to all Three Radars*

Those parts of the data selection and averaging routines common to all three radars were as follows. First, a selected experimental data type was chosen. Data types vary from radar to radar and sometimes even from experiment to experiment; they represent a specific data-acquisition and -analysis algorithm used to produce the archived data. Second, an average elevation and azimuth angle was calculated for each record and key parameters were selected, such as date, time, altitudes, and densities. Third, records below a set elevation angle were discarded (this step was not applicable to Arecibo data). Fourth, a routine eliminated all those densities not lying between 100-500 km and then linearly interpolated the remaining values to create a profile with 10 km spacing. Actually, because the data is stored in LOG format and it tends to be distributed exponentially in altitude, the interpolation is a linear interpolation of LOG density values. Finally, these individual profiles are grouped and averaged-- because this step varies from radar to radar, it will be discussed separately in the next three sections.

### *3.2.2 Sondrestrom Processing*

The data used at Sondrestrom came from fixed position records with the exception of June 1987 which was taken from elevation scan records. Fixed-position scans were normally eleven-position patterns like that shown in Figure 6. Similar nine-position

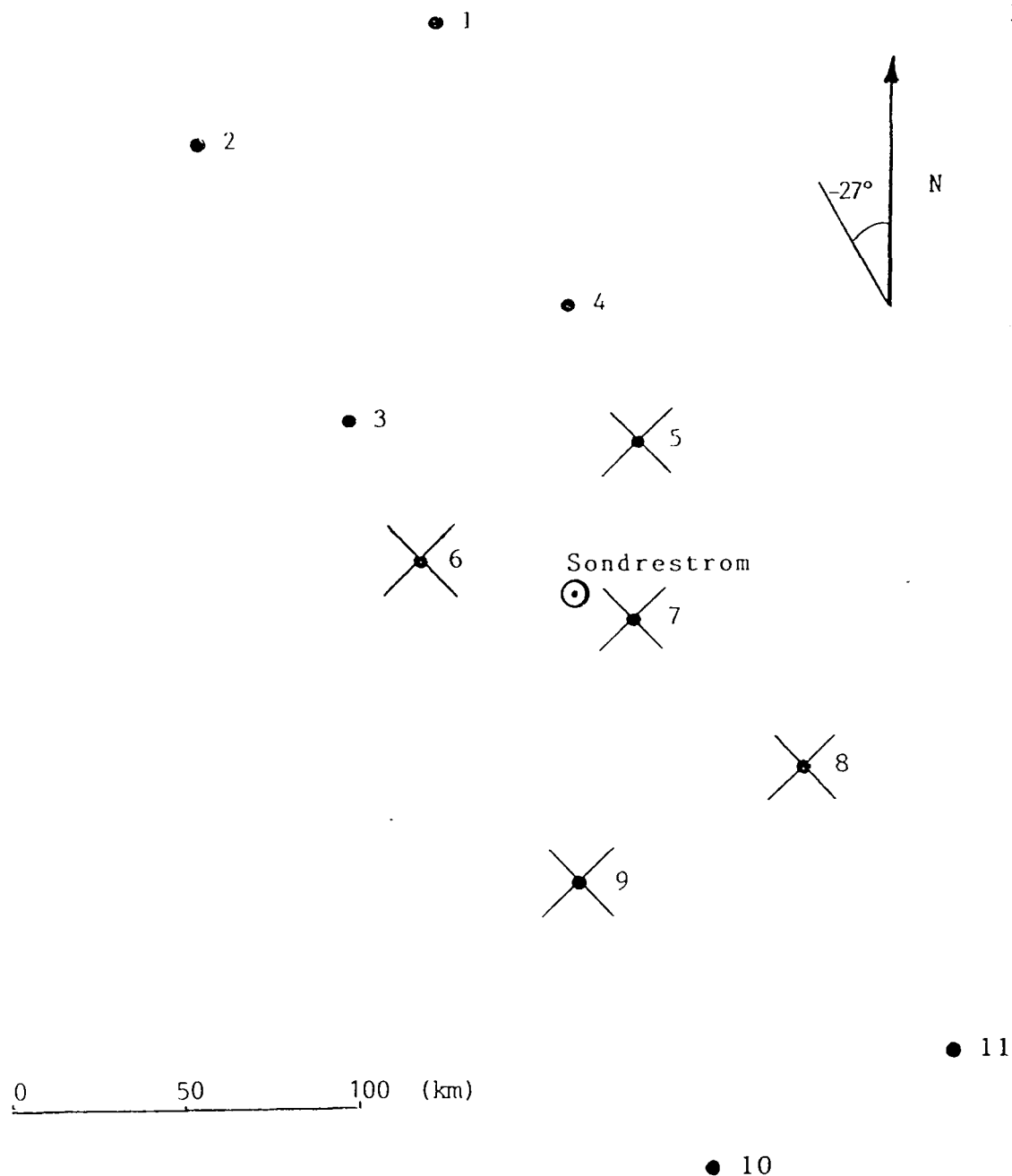


Fig. 6. Typical azimuthal pattern used for a fixed position Sondrestrom scan. Points represent the location of data at 100 km altitude. Dots (·) represent datum not selected for the average because of low elevation angles, whereas x's (x) represent datum used for the average. The scale is 2" = 100 km.

patterns, and patterns with an added parallel-to-B observation, were also used. Elevation scans used in the June 1987 experiment consisted of records whose densities were derived as the antenna was sweeping in elevation. Both fixed-position and elevation-scan patterns are approximately aligned on the local magnetic invariant meridian.

The averaging routine used for the fixed-position records grouped profiles by azimuthal pattern and then performed a simple average. There were at least five, and as many as seven, profiles per grouping. The elevation cutoff angle used for all Sondrestrom data was  $49^\circ$ . The averaging routine used for the one elevation-scan for June 1987 was processed in the same way as the Millstone data which is described below.

### *3.2.3 Millstone Processing*

At Millstone, different azimuthal patterns were used for nearly every experiment. Rather than writing a different routine for each one, I grouped the data by time alone. I found that a re-occurring pattern could be selected by simply sorting by time gaps between groups. Because of the variety of experiments, the number of averaged profiles ranged from 1 (no averaging) to 11. Most of the elevation-cutoff angles were at  $58^\circ$ , the lowest used was  $40^\circ$  for the Jun 1984 experiment.

### *3.2.4 Arecibo Processing*

For Arecibo records, the antenna pattern was fairly constant. Elevation angles were fixed at  $75^\circ$ , and the azimuthal pattern generally started with the first record at  $180^\circ$ , and successive records located every  $20\text{-}30^\circ$  in clockwise increments until  $180^\circ$  azimuth was again reached. The full  $360^\circ$  pattern was then repeated with a counterclockwise rotation.

The averaging routine used for these records grouped them so as to encompass a full clockwise or counterclockwise rotation, usually containing between 8 and 14 separate profiles. If a group contained significantly more profiles than this (I picked 21 as significant), it meant that the azimuths for successive records were not changing and I would delete this group to prevent biasing the data (note this was relatively rare). In a small subset of cases, a group would not cover a full  $360^\circ$  (usually only  $270^\circ$ - $350^\circ$ ); I did not think this would significantly bias the average and included these groups.

### 3.3 Running the TDIM Model

#### 3.3.1 Description of the Model Runs

Model data used for both Millstone and Sondrestrom came from existing data sets. These data sets were made to reproduce seasonal ionospheric parameters for low, medium, and high solar cycle and geomagnetic conditions, (By) positive and negative convection patterns; and for latitudes above  $50^\circ$  invariant. Therefore, runs were made without using the coupled low-latitude model. In addition, rather than including a coupled electron energy equation (with non-quantifiable heat inputs); daytime and nighttime  $T_e$  profiles as described by *Roble* [1975] were used while the auroral oval  $T_e$  profile as described by *Roble and Rees* [1977] was used. Finally, neutral composition inputs from MSIS were not varied with geomagnetic activity ( $A_p$  or  $K_p$ ) but were chosen based on a constant ( $A_p$ ) of 20.

This same TDIM-subset was used for Arecibo. Arecibo runs were only made for the solar and geomagnetic range applicable to a given experiment, and were only solved for

density. In addition, neutral-composition inputs from MSIS (for Arecibo runs) did vary with geomagnetic activity (Ap or Kp).

### *3.3.2 Seasonal, Solar Cycle, and Geomagnetic Definitions*

The following definitions were used for model input parameters:

a. Seasonal

Winter = 357 (Julian day)

Equinox = 82

Summer = 173

b. Solar Cycle

Maximum = 210 (F10.7 Flux)

Medium = 130

Minimum = 70

c. Geomagnetic

High = 6 (Kp index)

Medium = 3.5

Low = 1

Notice that the spring equinox seasonal input was used in the comparison for both spring and fall equinox observational conditions. In addition, two asymmetrical polar convection patterns were used, they were classified as By+ or By-.

Input parameters for each "World Day" were selected with observed geomagnetic (Kp) and solar (Sa) values as guides. In many cases, when the input parameter

classification was not clear, several model runs were made. Table 4 shows daily geomagnetic and solar data valid for the period of this study.  $\overline{Kp}$  values are derived by averaging daily Ap and then converting to Kp with a conversion taken from *Knecht and Shuman* [1985].  $\overline{Sa}$  values are a simple arithmetic mean of daily Sa. The Sa parameter is defined as the F10.7 solar flux normalized to one astronomical unit-- F10.7 and Sa flux are equivalent parameters for purposes of this study. Kp and Sa data for this table was taken from monthly published geophysical data, see for example *Coffey and references therein* [1984].

TABLE 4. Observed Solar and Geomagnetic Data

Date	Kp	$\overline{Kp}$	Sa	$\overline{Sa}$
<b>Jan. 1984</b>				
17	2		95.2	
18	2-		95.0	
19	3+		93.4	
		2+		94.5
<b>Mar. 1984</b>				
7	4	4	105.0	105.0
<b>Jun. 1984</b>				
26	2		100.1	
27	2+		101.5	
28	4-		99.5	
		3-		100.4
<b>Jul. 1984</b>				
23	2		87.3	
24	3-		86.8	
25	2		85.9	
		2+		86.7
<b>Sep. 1984</b>				
19	5-		74.6	
20	4-		74.1	
21	2+		75.1	
		4-		74.6
<b>Jan. 1985</b>				
15	2+		72.4	
16	2		74.7	
17	2+		75.8	
18	2-		74.1	
		2		74.3
<b>Mar. 1985</b>				
19	2+		74.2	
20	1+		74.2	
21	1+		76.1	
22	1		75.9	
		2-		75.1
<b>Jun. 1985</b>				
25	3-		71.0	
26	4-		70.0	
		3		70.5
<b>Jan. 1986</b>				
14	1		76.4	
15	1+		75.1	
16	1-		75.5	
17	2-		74.4	
		1		75.4

TABLE 4 Continued.

Date	Kp	$\overline{Kp}$	Sa	$\overline{Sa}$
Mar. 1986				
5	2		90.5	
6	4+		89.7	
		3+		90.1
Sep. 1986				
23	5-		68.7	
24	4-		68.8	
25	4		69.4	
26	4		68.5	
		4		68.9
Jan. 1987				
27	2		69.9	
28	3-		70.8	
29	2+		70.6	
30	1		69.8	
		2		70.3
Mar-Apr. 1987				
31	1		71.9	
1	2+		72.5	
		2		72.2
Jun. 1987				
1	2		77.8	
2	2		77.9	
3	1		76.4	
4	2-		77.3	
5	2		76.1	
		2		77.1
Jan. 1988				
12	4-		108.1	
13	2		113.7	
14	5		112.4	
15	6-		121.8	
16	1+		116.4	
		4		114.5
Mar. 1988				
16	3		114.1	
17	2+		117.4	
18	2		116.1	
19	1		116.1	
20	2-		116.3	
		2		116.0
Jun. 1988				
13	2-		115.0	
14	3+		111.7	
		3-		113.4



## CHAPTER IV

### ANALYSIS OF DATA

The color plates used for this analysis are only a subset of the 17 "World Day" cases covered in this study. They were chosen to represent key trends found throughout the data set. My primary emphasis in the analysis of plates 1 - 10 is to compare major ionospheric density features found for a cross-section of these "World Day" experiments. The remaining plates highlight the various trends found in this study or address a specific problem. A summary of the most significant trends can be found in the next section.

At this point, I would like to expand on the meaning of two terms used throughout this analysis. The first is "clutter echo" or "clutter" used in reference to coherent echo returns which contaminate some of the low altitude Millstone observations. The second is "tidal structure" or "tidal feature" used in reference to density perturbations in the observed diurnal variation of NmF2 and HmF2, primarily at Arecibo.

Clutter echoes are powerful coherent return-signals which appear in the radar sidelobes. These echoes occur mainly when the radar is operating at low altitudes, low-elevation angles, and when azimuths are north of Millstone; in addition, they are more common during relatively high geomagnetic activity. While clutter is prevalent for the above conditions, it is not limited to them. For example, clutter is also observed (although less frequently) for all elevation angles, azimuths, and levels of geomagnetic activity. These echoes physically arise from high-amplitude wave-induced plasma instabilities and are only observed when the radar-wave is nearly perpendicular to the

earth's magnetic field. The reason this feature does not appear at Arecibo is because of a lack of instabilities large enough to contaminate the sidelobes there. At Sondrestrom, where the geomagnetic dip angle is  $80^\circ$ , radar-wave/magnetic-field perpendicularity is not possible, therefore clutter echoes are not seen there. For a detailed explanation and analysis of Millstone clutter see *St-Maurice et al.* [1989].

Tides are perturbations on the diurnal thermospheric wind pattern. They are driven primarily by solar heating through differential absorption of solar EUV by the neutral constituents of the thermosphere, solar UV by ozone in the mesosphere, and solar-visible and -infrared radiation by water vapor in the troposphere. This differential heating effect sets up tides which exhibit diurnal, semidiurnal, and possible higher order modes. In addition, the various tidal modes are highly latitude dependent. It is the semidiurnal mode and some lesser composite modes that are prevalent at Arecibo [*Crary and Forbes*, 1986]. Tides are not as important at Millstone and Sondrestrom because of this latitude dependence [*e.g.*, *Salah*, 1974; *Fesen et al.*, 1986; and *Forbes*, 1987].

Plates are formatted as follows. First, the bottom (horizontal) axis represents universal time (UT) with a conversion to local time (LT) normally shown on the top horizontal axis. Second, the vertical axis represents altitude from 100 - 500 km. Third, black areas in the plates represent either density values off the scale of the plot, times when the radar was not operating, or data from lower altitudes which was not supplied. Fourth, clutter echoes for low altitudes at Millstone were not subtracted from the observations. Discussion of the plates follows.

## 4.1 Plate 1, Comparison of 17-19 Jan 1984

In general, the model-produced density-patterns agree with observed values. The agreement is better at Sondrestrom and Millstone than at Arecibo. In addition, tidal structure is evident in the Arecibo observations and is not reproduced by the model.

### 4.1.1 *Sondrestrom Comparison*

- a. NmF2 pattern is very similar.
- b. Daytime HmF2 values produced by the model are about 25 km higher than observed by the radar.
- c. The diurnal phase is reproduced almost exactly by the model. However, there is an asymmetrical structure around daytime-maximum values that is not in the observations. This feature was found to be due entirely to the input (By) component.

### 4.1.2 *Millstone Comparison*

- a. The NmF2 and HmF2 pattern is very similar.
- b. The diurnal phase is extremely close with the exception of a secondary evening peak found in the observations on the second day and centered on 22 UT.

### 4.1.3 *Arecibo Comparison*

- a. Maximum daytime NmF2 values are 3-4 times higher in the observations than found in the model. The nighttime peak values are similar.



- b. The height of daytime peak-density values is about 25 km higher in the model. Early in the night HmF2 is nearly the same, but by 8 UT it is about 50 km higher in the model.
- c. The diurnal phase of daytime features is very good. However, the nighttime pattern is not well produced.

## **4.2 Plate 2, Model Sensitivity to Kp - An Alternate Model Comparison of 17-19 Jan 1984**

This plate was made to show the model sensitivity to the geomagnetic input (Kp), it is identical to the previous plate except that the model input here is  $K_p = 1$ . The actual conditions for this day made it difficult to classify this input parameter (see appropriate values in Table 4). It is apparent when comparing this plate with the previous plate that Kp has little effect on Millstone and Arecibo, but greatly effects Sondrestrom.

### *4.2.1 Sondrestrom Comparison*

- a. The NmF2 and HmF2 variations look very similar.
- b. The diurnal phase is again reproduced almost exactly, but this time without the asymmetry noted in Plate 1. This demonstrates the model sensitivity to Kp at high latitudes-- not only does this asymmetry depend on input Kp but it also depends heavily on the chosen (By) component.

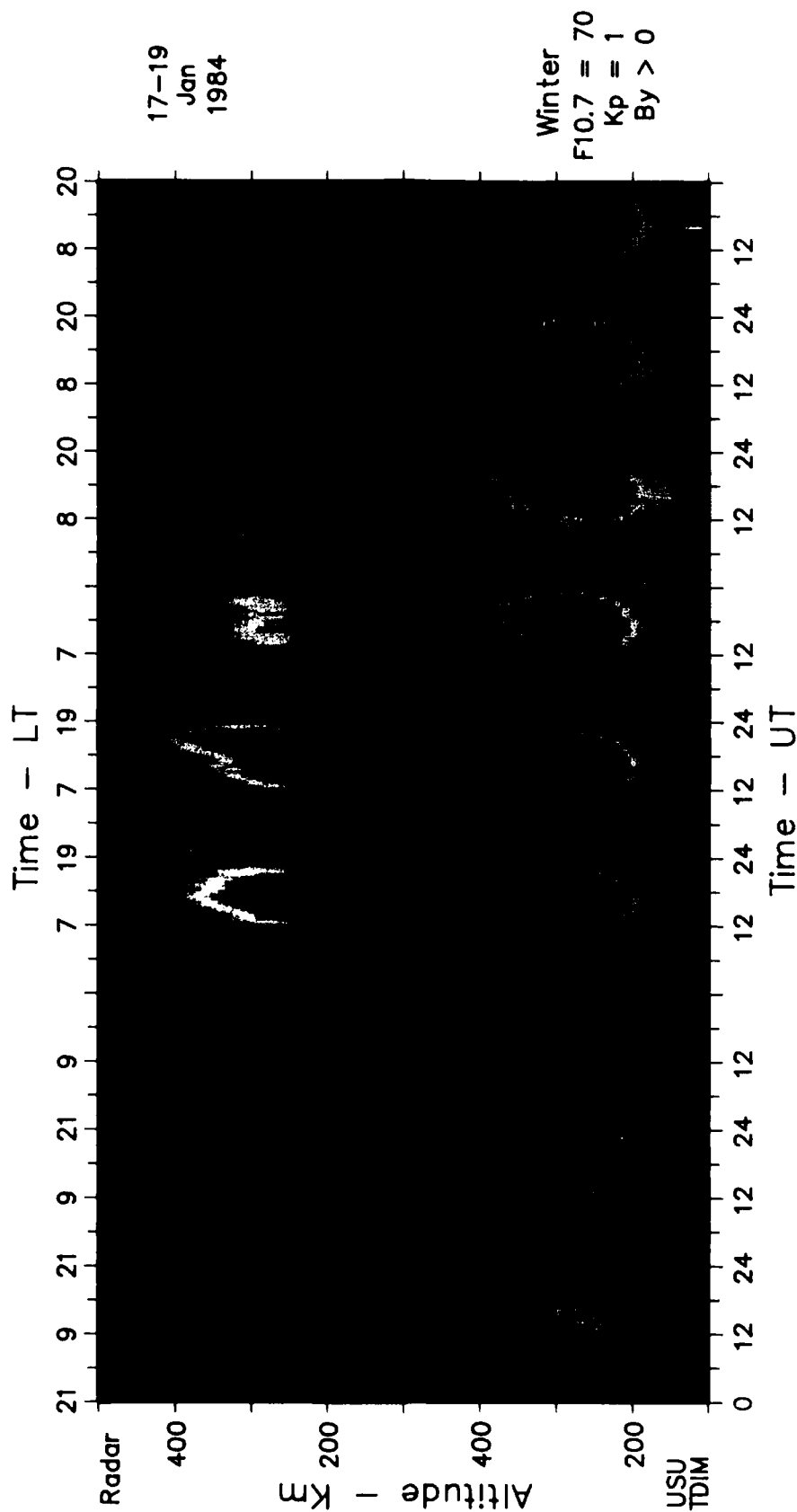
### *4.2.2 Millstone Comparison*

- a. The entire pattern has not really changed from the previous case.

SONDRESTROM

MILLSTONE

ARECIBO



#### 4.2.3 Arecibo Comparison

- a. Again the entire pattern is similar to the previous plate.

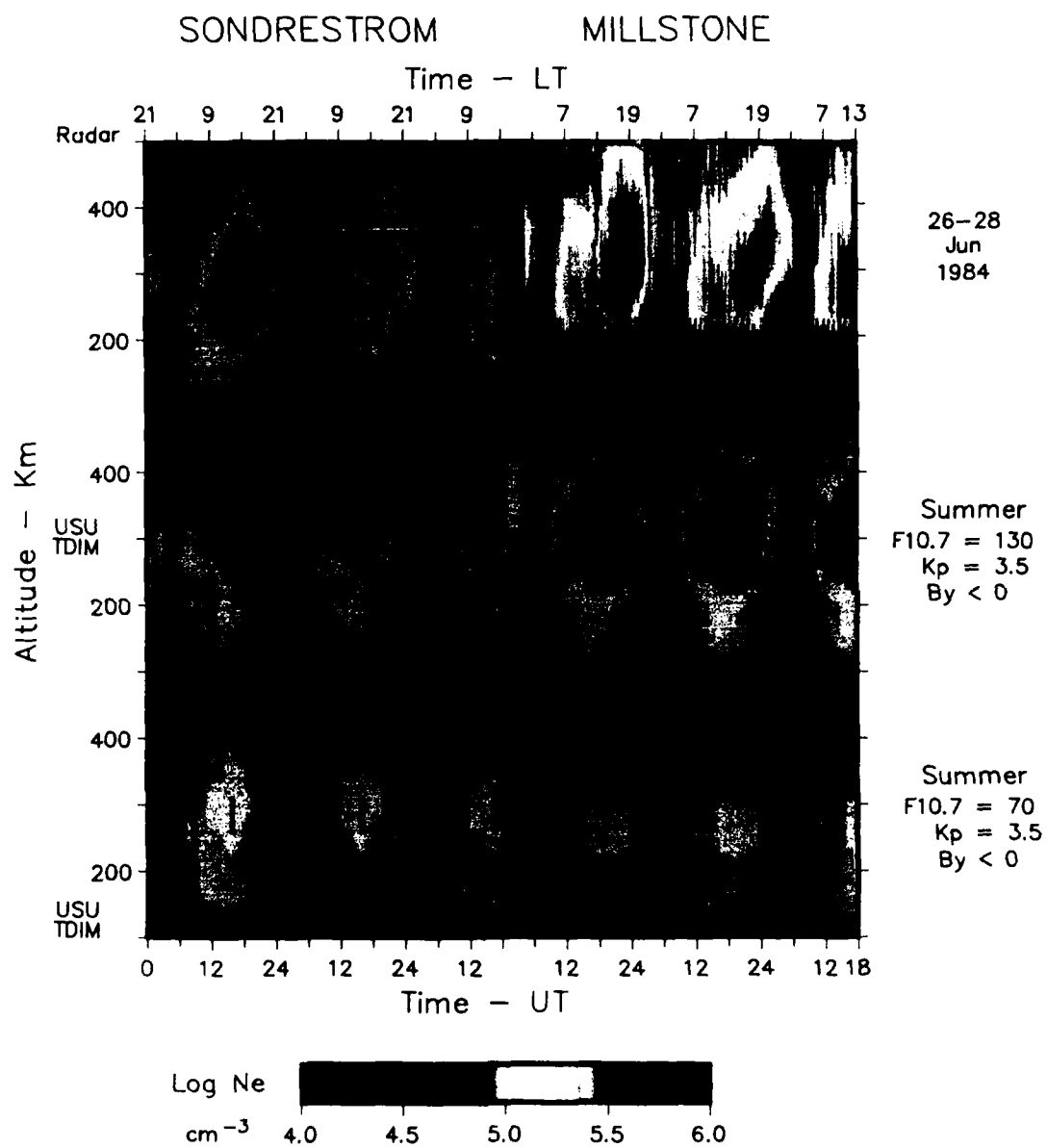
### 4.3 Plate 3, Model Sensitivity to F10.7 - Comparison of 26-28 Jun 1984

The main purpose of this plate is to show the sensitivity of the model to the solar-flux input (F10.7); and to demonstrate the importance of using multiple radars to constrain model inputs used in the comparisons. Observed values of the solar flux (Sa) for this "World Day" case make it difficult to classify this input for the model (see appropriate values in Table 4).

The model runs at Millstone and at Arecibo (Arecibo is not shown) seem to constrain  $F10.7 = 130$ . This however produces high daytime HmF2 at Sondrestrom. This could be due to a high-latitude difference in neutral winds from those input to the model. A model run with  $F10.7 = 100$  would be useful in any further analysis of this case.

#### 4.3.1 Sondrestrom Comparison

- a. The daytime- and nighttime-maximum values of NmF2 are very similar for the case of  $F10.7 = 130$ .
- b. When  $F10.7 = 70$ , the NmF2 are a little low but not significantly so.
- c. Nighttime values of HmF2 are similar for both cases of F10.7.
- d. Daytime-observed and -modelled values of HmF2 are similar when F10.7 was set to 70. However, for  $F10.7 = 130$  these model HmF2 levels are approximately 75 km higher than the observed values.





- e. The diurnal-phase variation was very close in both cases except that the model does not reconstruct the rapid nighttime disappearance of the F2-layer.

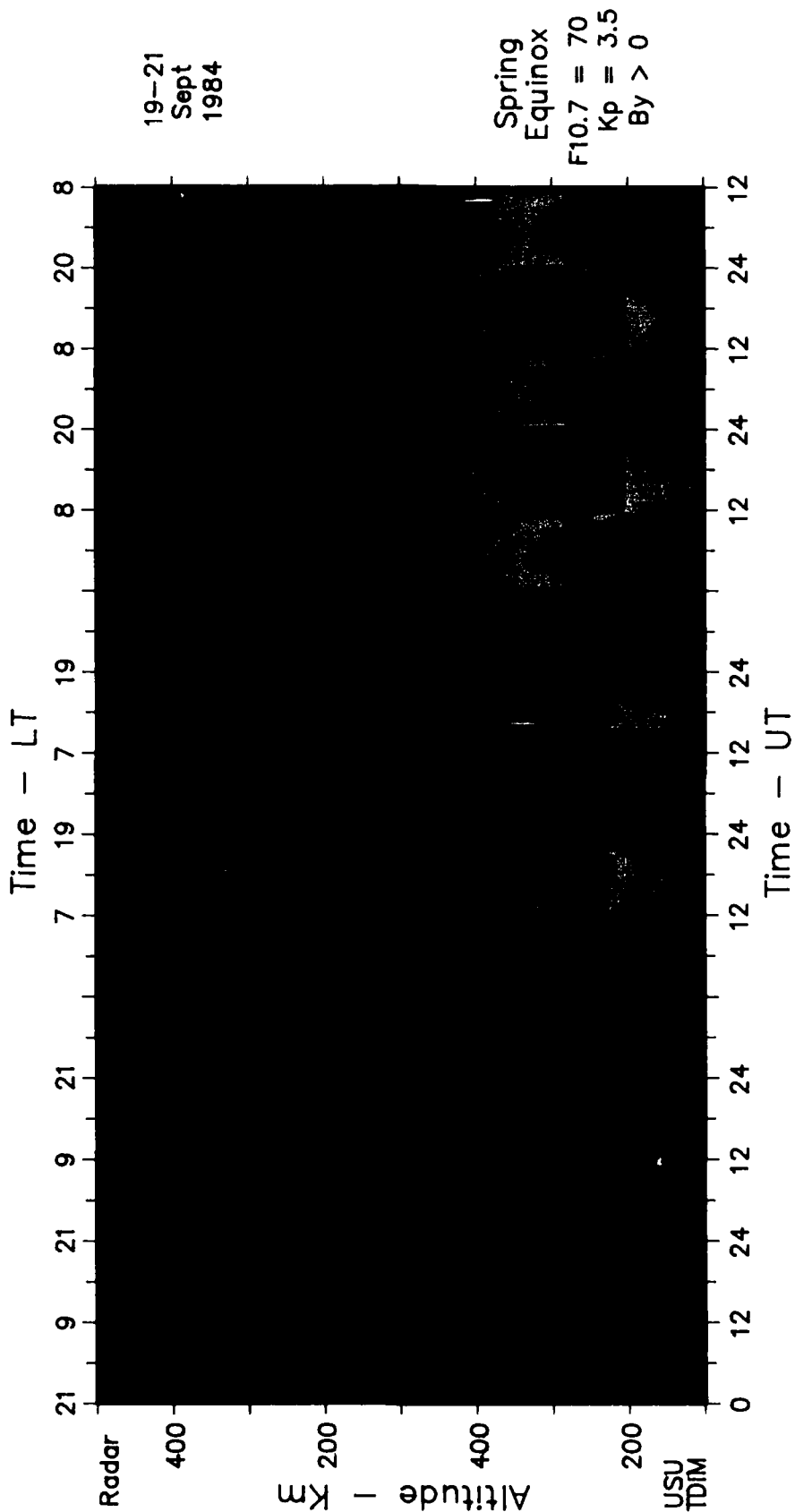
#### 4.3.2 Millstone Comparison

- a. Daytime- and nighttime-maximum values of NmF2 are remarkably close for the  $F_{10.7} = 130$  case. When  $F_{10.7}$  is set to 70, the model-produced maximum-NmF2 is about 1/4 of the observed value.
- b. When  $F_{10.7} = 130$ , both daytime- and nighttime-HmF2 values are remarkably similar. When  $F_{10.7}$  is set to 70, the model produces HmF2 levels about 25 km lower than observed.
- c. The model-produced diurnal-phase for both cases of  $F_{10.7}$  is similar to that in the radar observations. However, both model-runs fail to pick up a late-afternoon secondary-peak observed by the radar.

### 4.4 Plate 4, Comparison of 19-21 Sep 1984

There appears to be mixed results for this fall equinox "World Day" case. While agreement is remarkable at Millstone, Sondrestrom and Arecibo are not as good. At Sondrestrom, the effect of running a spring-equinox day for a fall-equinox comparison is probably the main cause for the marginal reproduction of radar observations. In addition, auroral structure has not been reproduced by the model. Discrepancies found at Arecibo are similar to those found there in other seasons.

# SONDRESTROM      MILLSTONE      ARECIBO



#### *4.4.1 Sondrestrom Comparison*

- a. Daytime-maximum NmF2 is slightly higher in the model than for the observations (model values are less than 1/2 as large). Nighttime values of NmF2 are similar.
- b. Heights associated with maximum-daytime and -nighttime NmF2 are similar except for an apparent lowering of the layer (around 18 UT) in the observations which is not reproduced by the model.
- c. The overall appearance of the comparison is marginal. The daytime model peaks are created in the right time intervals, but the distribution of densities away from HmF2 is not the same, and aurorally produced structure in the observations is missing in the model.

#### *4.4.2 Millstone Comparison*

- a. The overall reproduction of NmF2 is remarkable, the only exception is a trough apparent during the second night of radar observations that is not reproduced by the model.
- b. HmF2 variations are very well reproduced.
- c. The diurnal phase and overall pattern look extremely good with the exception of a secondary evening peak in the observations.

#### *4.4.3 Arecibo Comparison*

- a. Observed-daytime peak-density values are 3-4 times larger than in the model while nighttime-NmF2 values are closely reproduced.

- b. The daytime-HmF2 pattern matches observations. The nighttime pattern is reasonable except for the failure of the model to reproduce the rapid fall of F2-layer in the early morning hours.
- c. The timing of most features is closely reproduced except for that mentioned in (b).

## 4.5 Plate 5, 15-18 Jan 1985

In general, the model reproduction for this experiment is very good, especially at Sondrestrom and at Millstone. The biggest discrepancies include the failure of the model to reproduce auroral structure at Sondrestrom and daytime NmF2 at Arecibo.

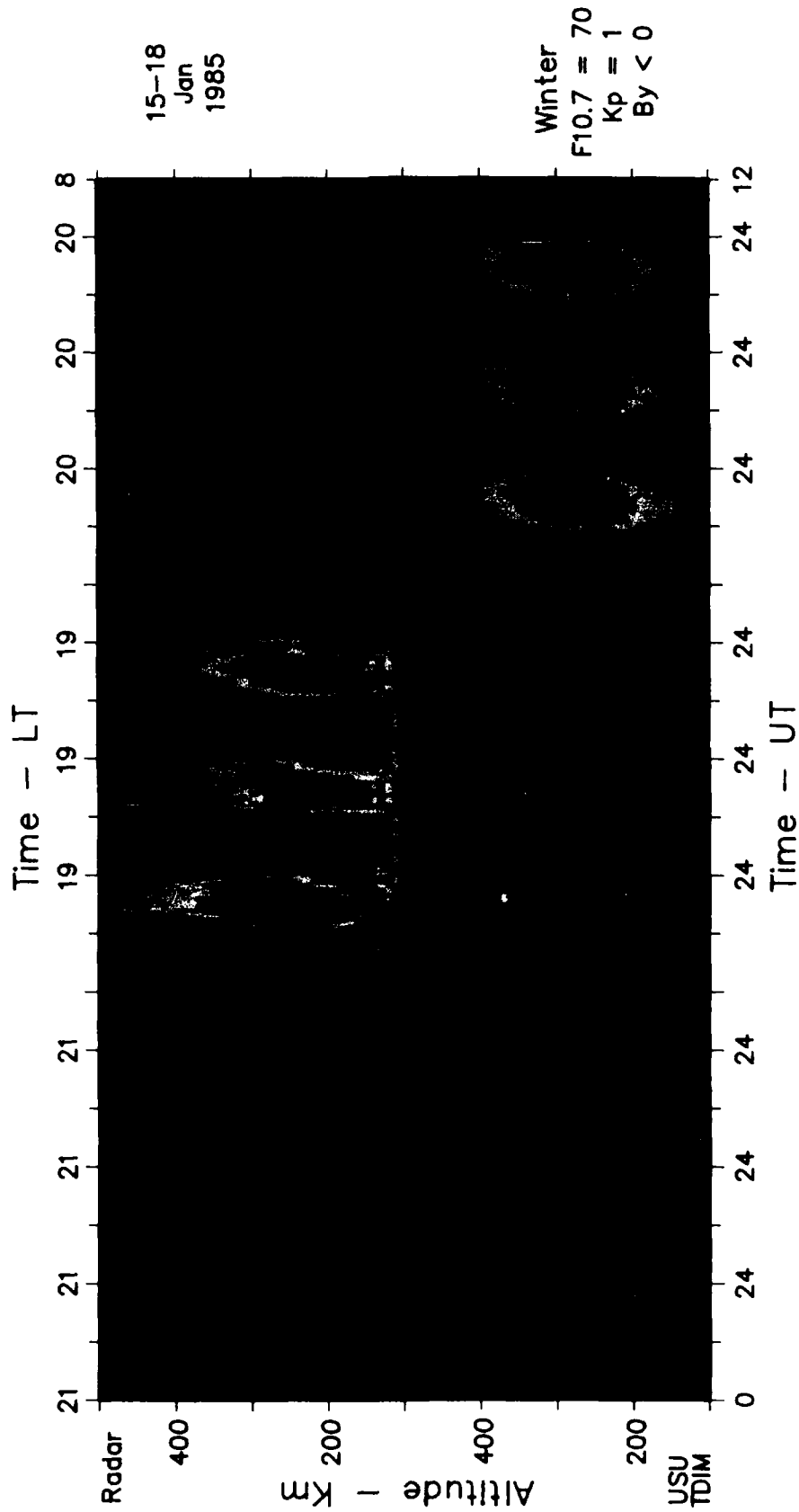
### 4.5.1 *Sondrestrom Comparison*

- a. Model reproduced NmF2 and HmF2 are very close.
- b. Timing of the density pattern is reproduced almost exactly.
- c. Auroral structure is evident in the radar observations which is not reproduced by the model.

### 4.5.2 *Millstone Comparison*

- a. NmF2 and HmF2 values are very close. However, during the first day of the experiment, the radar-observed daytime peak-densities are twice as high as those in the model. These higher densities for that day are also observed at Arecibo although not at Sondrestrom. Solar and geomagnetic indicators do not reflect a reason for this higher activity on that day (see Table 4).

SONDRESTROM      MILLSTONE      ARECIBO



- b. Model reproduction of the diurnal phase is very good, but it again fails to pick up a secondary evening peak found in the observations.
- c. Low-altitude clutter is evident in these Millstone observations.

#### *4.5.3 Arecibo Comparison*

- a. Maximum daytime densities are 3-4 times higher in the observations than in the model. The highest densities are found during the first day.
- b. Nighttime NmF2 values are similar except during the second night of the experiment where observed densities are twice as high as in the model.
- c. Daytime HmF2's are close while nighttime values vary because observed densities exhibit tidal structure not produced by the model.
- d. The timing of the diurnal pattern looks good except that the model does not reproduce the rapid early-morning fall of the F2-layer.

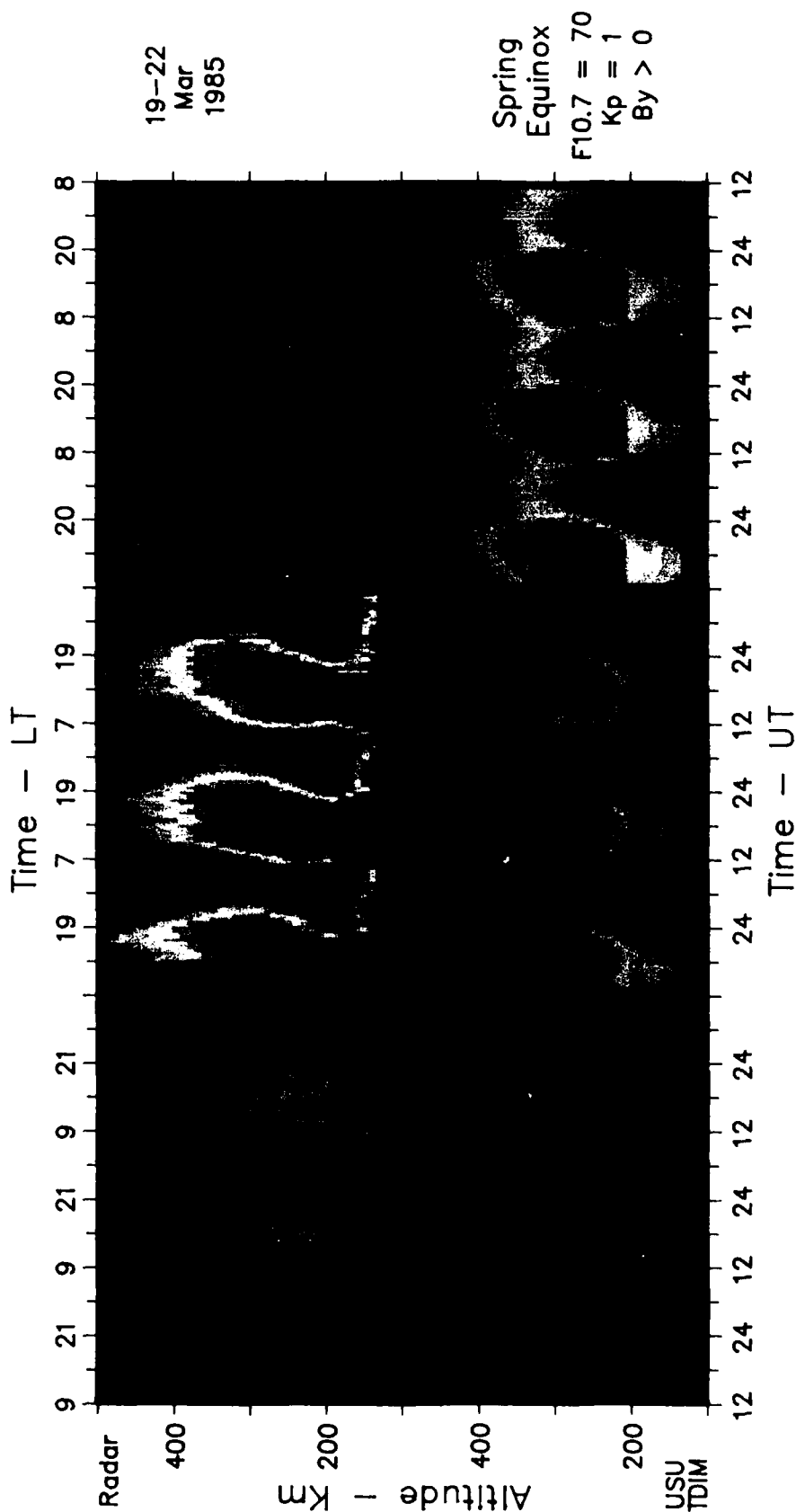
### **4.6 Plate 6, 19-22 Mar 1985**

Overall reproduction of observations for this day is very good. The only significant exception is the failure of the model to reproduce correct daytime NmF2 values at Arecibo. In addition, there is structure at all three radars which is not reproduced by the model.

#### *4.6.1 Sondrestrom Comparison*

- a. Daytime- and nighttime-NmF2 values are almost exactly reproduced.

# SONDRESTROM      MILLSTONE      ARECIBO



- b. While nighttime HmF2's are close, even though hard to discern, daytime modelled HmF2's are approximately 25 km too high.
- c. Diurnal timing looks good, however the model fails to reproduce a second-daytime maximum found on the 21st.
- d. Daytime and nighttime structure is very visible in the observations and is not reproduced by the model.

#### *4.6.2 Millstone Comparison*

- a. Daytime NmF2's are slightly higher in the observations (less than twice as high). Nighttime NmF2's are about the same.
- b. Daytime HmF2's are about 25 km too high in the model.
- c. The diurnal pattern looks similar with the exception of a very minor secondary evening peak found in the observations.
- d. The overall structure of the observations is more complex and clutter is evident at low altitudes.

#### *4.6.3 Arecibo Comparison*

- a. Daytime NmF2's are up to 3 times higher in the observations than in the model. Nighttime-modelled values are similar to those in the observations.
- b. The variation of HmF2 with time shows a greater amplitude in the observations than in the model. Daytime-observed HmF2's start out lower than the model and then climb to nearly equivalent ranges by the end of the day. The observed nighttime-collapse of the F2-layer is much more dramatic



than in the model.

- c. There is considerable structure noted in the observations which is not reproduced by the model.

## 4.7 Plate 7, 14-17 Jan 1986

The overall model reproduction of observations was remarkably good for this case. However, the observations at all three radars are highly structured, particularly at night, and this is not reproduced by the model.

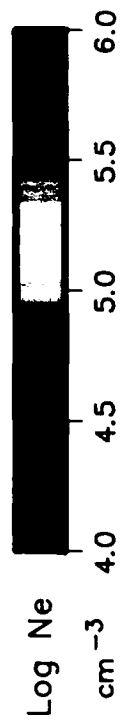
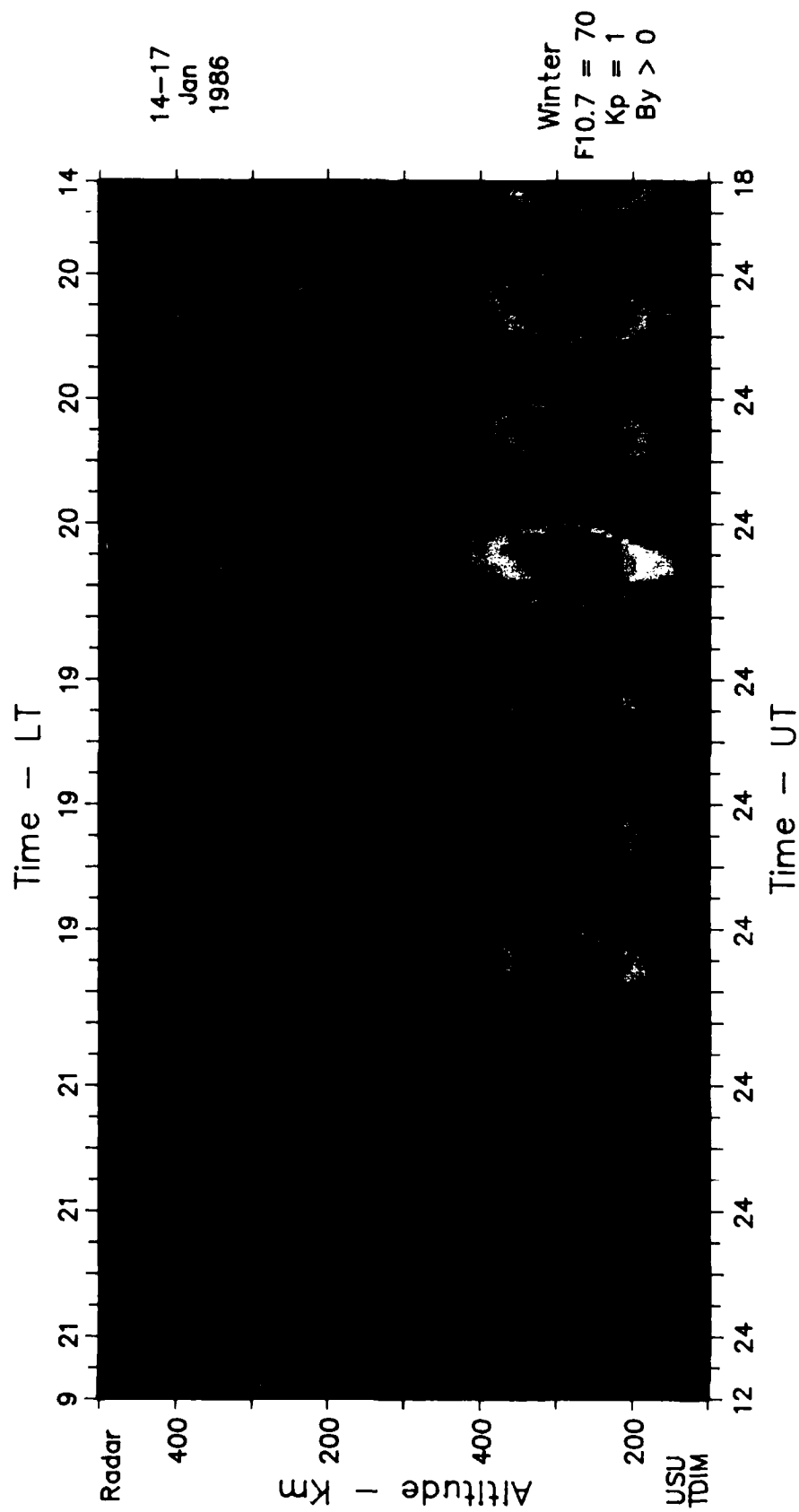
### 4.7.1 *Sondrestrom Comparison*

- a. In general, the NmF2 comparison is very good for both day and night conditions.
- b. Daytime-modelled HmF2 values are about 25 km too high. Nighttime-observed HmF2's are hard to locate because of the structure in the observations.
- c. The diurnal timing of the model is very good.

### 4.7.2 *Millstone Comparison*

- a. Daytime NmF2's are closely reproduced while nighttime model values are slightly lower (about a factor of 1/2).
- b. Daytime and nighttime HmF2's appear to be about 25 km too high in the model. Nighttime HmF2's are hard to locate in the observations because of structure.

SONDRESTROM      MILLSTONE      ARECIBO



- c. Timing of the diurnal pattern is closely reproduced by the model. The secondary evening peaks noted for many of the other "World Day" cases are not as evident here.
- d. The observational pattern is highly structured and clutter is evident at low altitudes. In addition, high- and low-altitude nighttime-densities are 2-3 times lower in the model than in the observations.

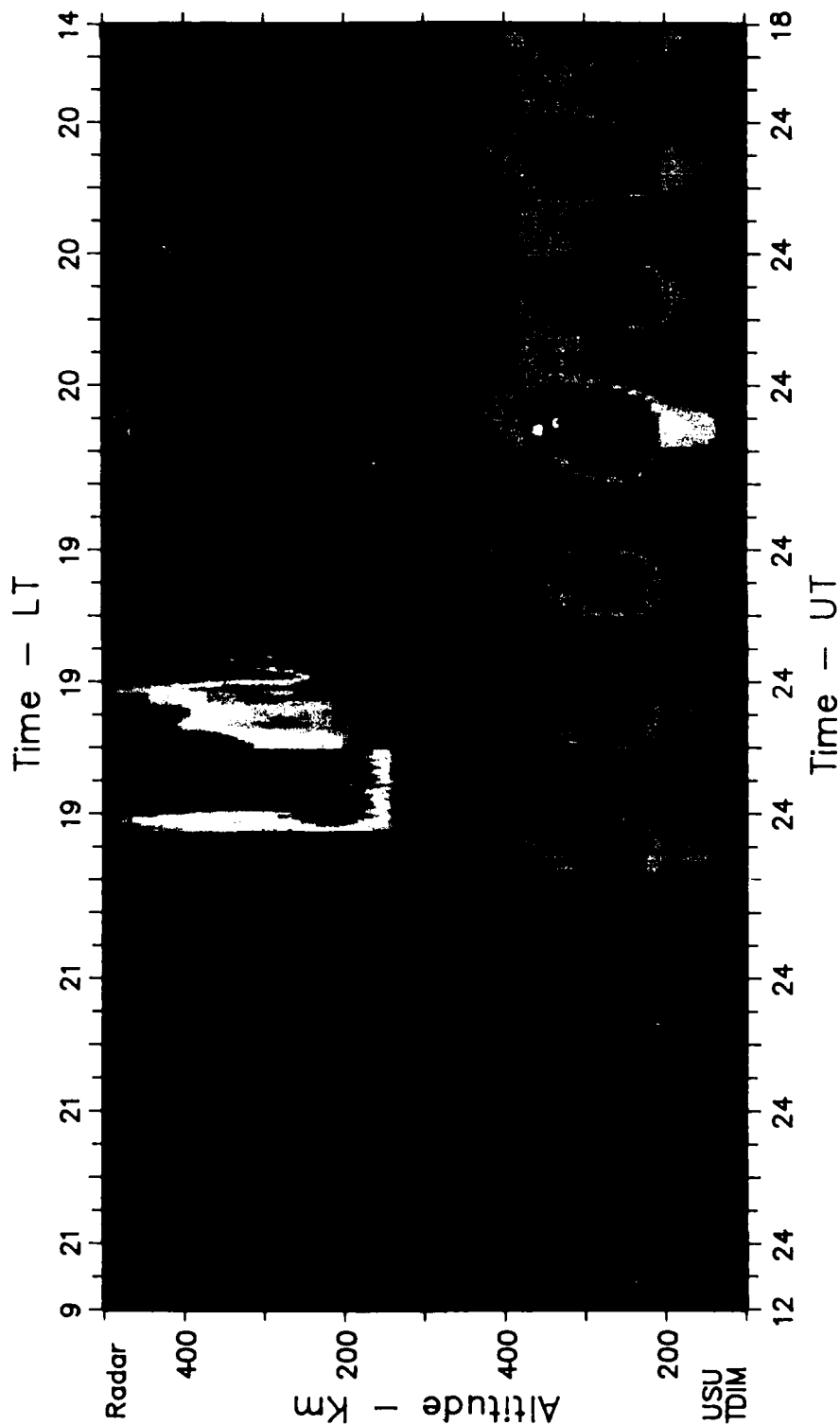
#### *4.7.3 Arecibo Comparison*

- a. In contrast to many of the other cases, daytime-NmF2 values are very similar. Nighttime values are also similar except where tidal structure is evident.
- b. *HmF2 locations are close during the day but are hard to compare at night because of structure in the observations.*
- c. The timing of the diurnal pattern is very closely reproduced by the model.
- d. A significant amount of tidal structure is evident in the observations both at night and during the day. This is not reproduced by the model.

### **4.8 Plate 8, 23-26 Sep 1986**

This fall equinox "World Day" comparison shows mixed results. The overall model-produced densities are very similar to Millstone observations, while Arecibo's daytime-NmF2 values are higher than in the model. The model reproduction of Sondrestrom densities is poor. This may be due to running a spring-equinox model-day to reproduce

# SONDRESTROM      MILLSTONE      ARECIBO



a fall-equinox pattern. In addition, Sondrestrom observations show significant structure due to auroral precipitation which is not reproduced by the model.

#### *4.8.1 Sondrestrom Comparison*

- a. Model-produced daytime NmF2's are slightly higher than observed (less than twice as high). The nighttime NmF2's are generally similar.
- b. The daytime HmF2 values are about 50 km higher in the model. Nighttime HmF2's are hard to compare because of structure in the observations.
- c. Nighttime densities at low and high altitudes are significantly lower in the observations than in the model.
- d. Diurnal phase shows much more structure in the observations than in the model. The overall pattern of the observed plot does not look like the model pattern.

#### *4.8.2 Millstone Comparison*

- a. NmF2's appear similar for both night and day conditions.
- b. HmF2's appear similar except for a secondary evening peak in the observations as well as an area of lower nighttime-observed densities at around 5 LT on the 24th.
- c. The diurnal timing looks good.
- d. There is significant clutter in the observations, particularly during the day on the 24th, where clutter effects are apparent as high as 300 km.

#### *4.8.3 Arecibo Comparison*

- a. Peak-daytime NmF2's are 2-4 times higher in the observations while nighttime values are similar.
- b. HmF2 variation is similar except that the model does not reproduce the rapid fall of the F2-layer in the early morning.
- c. Diurnal timing is similar.
- d. Observations are highly structured and this is not reproduced in the model.

### **4.9 Plate 9, 1-5 Jun 1987**

Model simulation for this summer "World Day" case is good at Sondrestrom but marginal at both Millstone and Arecibo. All three radars exhibit considerable structure throughout the period. Note that solar and geomagnetic observations for these days are not indicative of this observed structure (see Table 4).

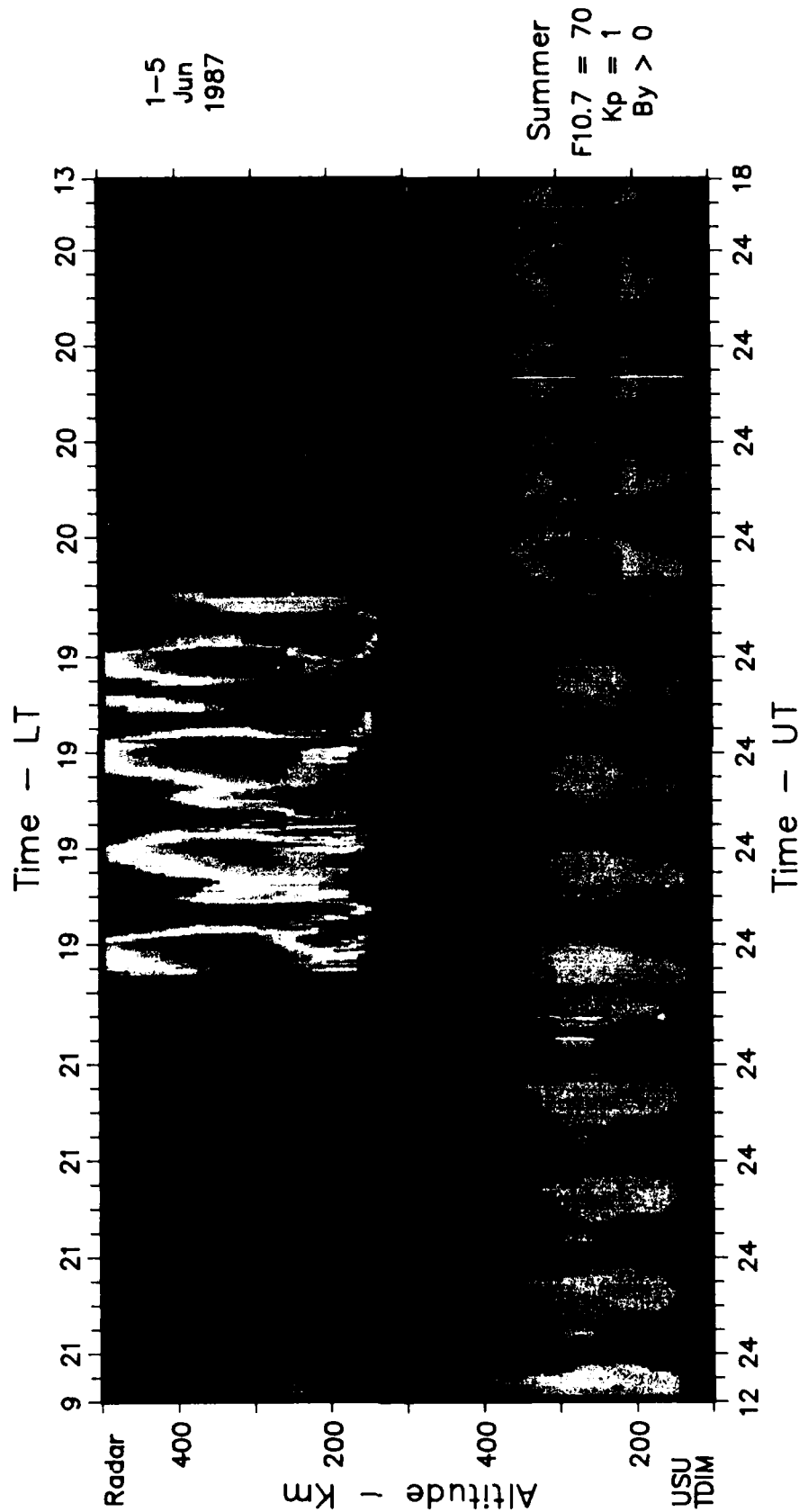
#### *4.9.1 Sondrestrom Comparison*

- a. Modelled- and observed-NmF2 values are similar for both daytime and nighttime conditions.
- b. HmF2 values are generally similar but the observations show considerably more structure in its variation with time.
- c. Timing is good for the major density features.

#### *4.9.2 Millstone Comparison*

- a. Daytime-maximum NmF2 values are 2-3 times higher in the model while

# SONDRESTROM      MILLSTONE      ARECIBO



nighttime values are similar.

- b. HmF2's for maximum-daytime NmF2 values are about 75 km higher in the observations than in the model. Nighttime levels are similar. There is considerable structure in the variation of HmF2 with time which is not reproduced by the model.
- c. For this case, the secondary peak noted in other Millstone "World Days" seems to be amplified. The peak values occur between 17-21 LT.
- d. Clutter is apparent throughout the low altitudes of the observations.

#### *4.9.3 Arecibo Comparison*

- a. Peak radar densities are off the plotted scale. There are very high NmF2's on 1 June, where peak values of LOG 6.6 ( $3.98 \times 10^6$ )  $\text{cm}^{-3}$  occur in the observations. The remaining days have peak values of LOG 6.1 ( $1.26 \times 10^6$ )  $\text{cm}^{-3}$ . An NmF2 of Log 6.6  $\text{cm}^{-3}$  is 16 times higher than the highest NmF2 produced by the model (LOG 5.4 or  $2.51 \times 10^5$   $\text{cm}^{-3}$ ). However, the peak observed densities for 2-5 June are only 4-5 times higher than those produced by the model.
- b. Model-daytime HmF2 values are approximately 50 km too low. Nighttime values are similar except for the rapid fall of the F2-layer in the early-morning hours.
- c. Timing for the onset of daytime production is correctly modelled. However, nighttime decay of NmF2 occurs too early in the model.
- d. Observations show some nighttime tidal activity which is not reproduced by



the model.

#### 4.10 Plate 10, 12-16 Jan 1988

The solar and geomagnetic conditions for this case are relatively active and changeable, see Table 4. The overall model reproduction for all three radars (at least on some of the days) is good with a slight over-production of densities at Sondrestrom and Millstone; and good agreement at Arecibo. There is a significant amount of structure at Sondrestrom and Arecibo which is not reproduced by the model.

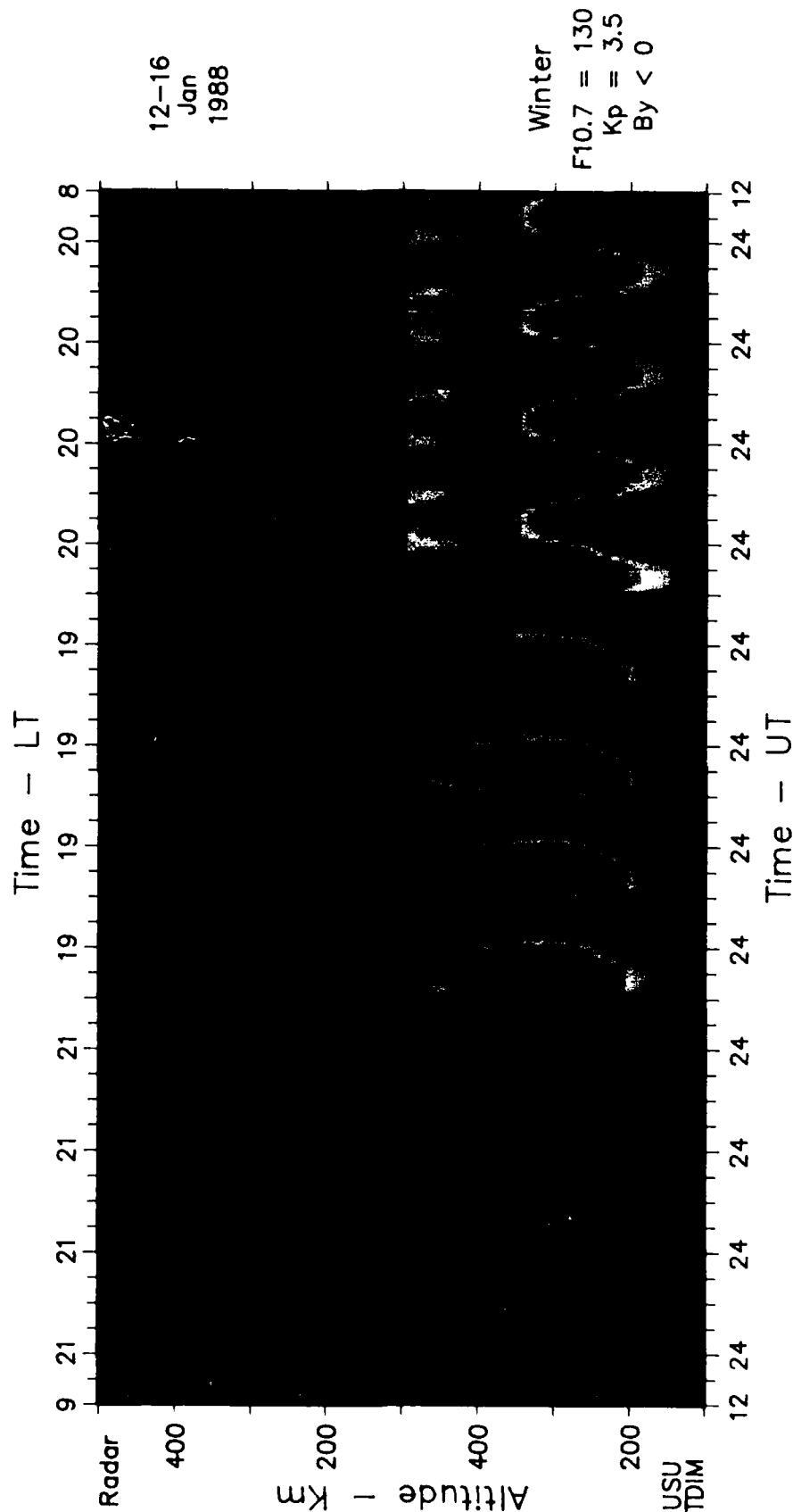
##### 4.10.1 *Sondrestrom Comparison*

- a. During the first two days, the peak-observed NmF2's are similar. The last 3 days show a slight overestimate of NmF2 by the model (about 2 times higher).
- b. Daytime- and nighttime-HmF2 values are similar for the first two days. After that, it is difficult even to discern a diurnal pattern in the observations.
- c. For the first 2 days-- timing of the diurnal pattern is good, the model even picks up the asymmetry in the observations.

##### 4.10.2 *Millstone Comparison*

- a. Both maximum-daytime and -nighttime NmF2 values are reproduced by the model.
- b. The daytime- and nighttime-model HmF2's appear to be about 25 km too high.

# SONDRESTROM      MILLSTONE      ARECIBO



- c. The diurnal pattern seems to be timed correctly.
- d. There are very high evening densities in the observations on 14 January, with very high NmF2 and HmF2 values.
- d. Clutter is not as apparent in this case as it was in others.

#### *4.10.3 Arecibo Comparison*

- a. Observed- and modelled-NmF2 values are in close agreement except for evening values on 14 January, which in the observations are as high as LOG 6.5 ( $3.16 \times 10^6$ ) cm<sup>-3</sup>.
- b. Generally, the modelled-HmF2 pattern is similar to the observations. However, there is a great deal of diurnal structure in the observed HmF2's which is not reproduced by the model.
- c. The timing of the diurnal pattern is very good.
- d. There are very high NmF2 and HmF2 values in the evening and early morning of 14-15 January-- like that observed at Millstone.
- e. There is a great deal of tidal structure in the observations that is not reproduced by the model.

### **4.11 Plates 11-12, Comparison of Spring and Fall Equinox**

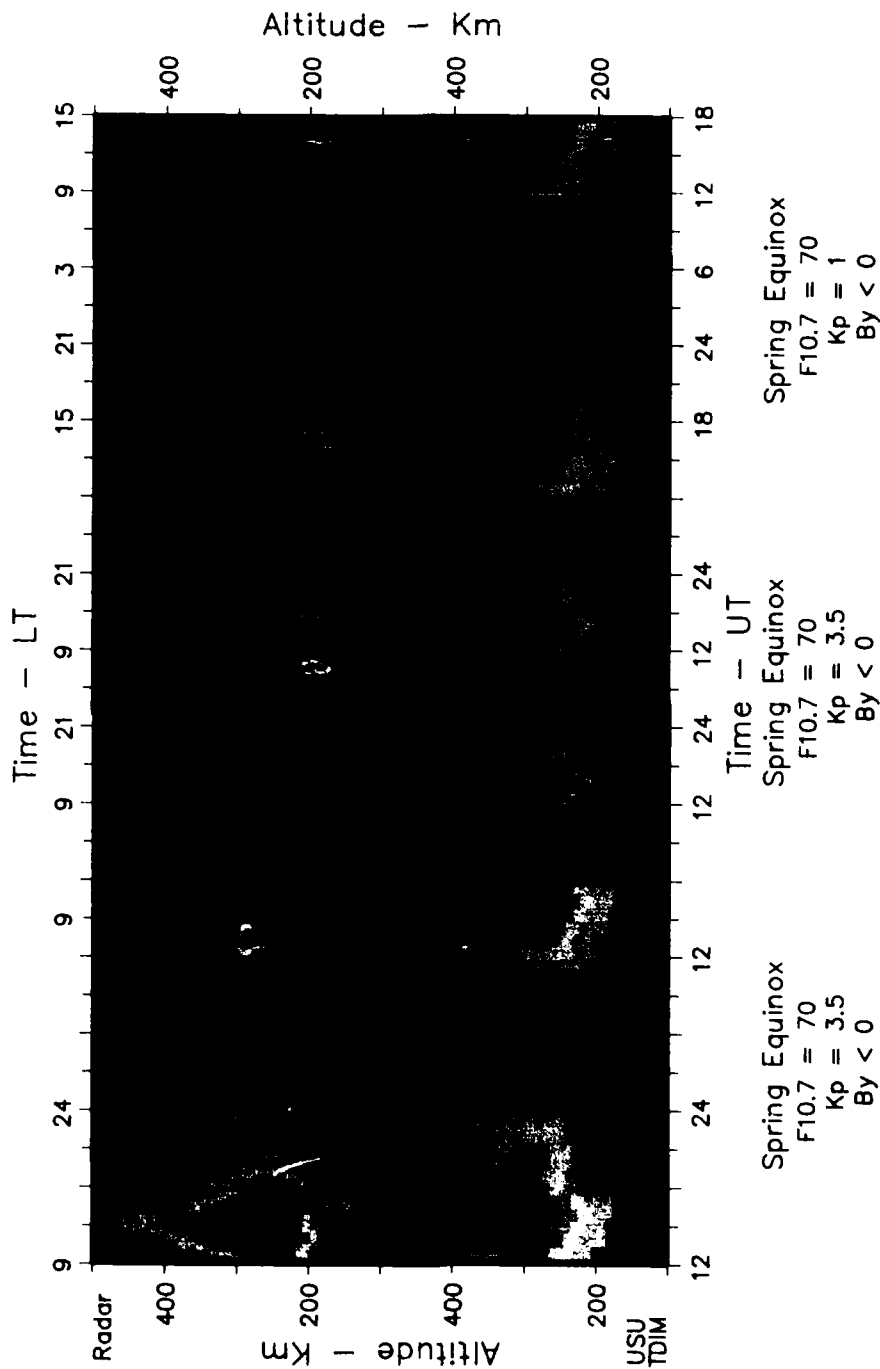
These two plates demonstrate the effect of using a spring-equinox day as a seasonal-input parameter to reproduce both spring- and fall-equinox conditions. In general, the

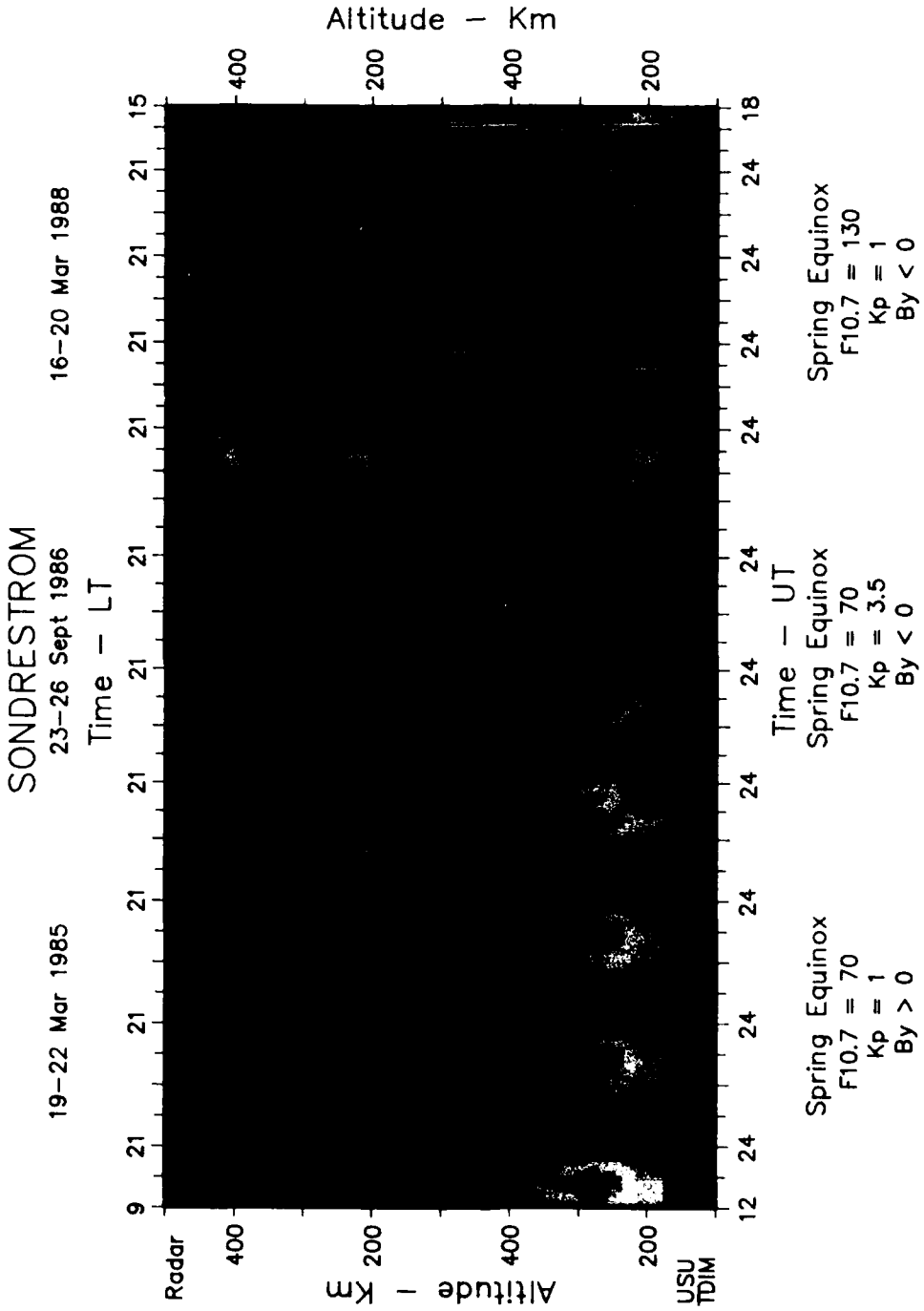
# SONDRESTROM

5-6 Mar 1986

19-21 Sept 1984

31 Mar--1 Apr 1987





agreement between radar and observations is very good for spring-equinox and is not for fall-equinox conditions. Sondrestrom was chosen for this comparison because the seasonal variations are larger there.

#### **4.12 Plate 13, Secondary Evening Peak at Millstone**

This plate emphasizes the secondary evening peak observed at Millstone which is not reproduced by the model. This condition is observed in the majority of cases studied and is most evident for summer and equinox conditions.

#### **4.13 Plates 14-16, High-Latitude Winter and Summer Cases with Geomagnetic Activity**

Plates 14 and 15 show a case in which radar observations indicated considerable geomagnetic activity, particularly on the last 3 days. Since observed-solar and -geomagnetic parameters were variable during this period, I varied those inputs in the model. These two plates contrast medium and high values of Kp to see if the observed Kp parameter is a good indicator of what is observed. It appears that a "best fit" occurs when the observed-solar and -geomagnetic parameters are most closely fit.

Plate 16 is a summer case with geomagnetic activity, especially on 28 June. If one contrasts this plate with plate 3, one again finds that even for an active day-- fitting the model with the observed-solar and -geomagnetic parameters will best reproduce the observations.

Plate 13. Secondary evening peak at Millstone



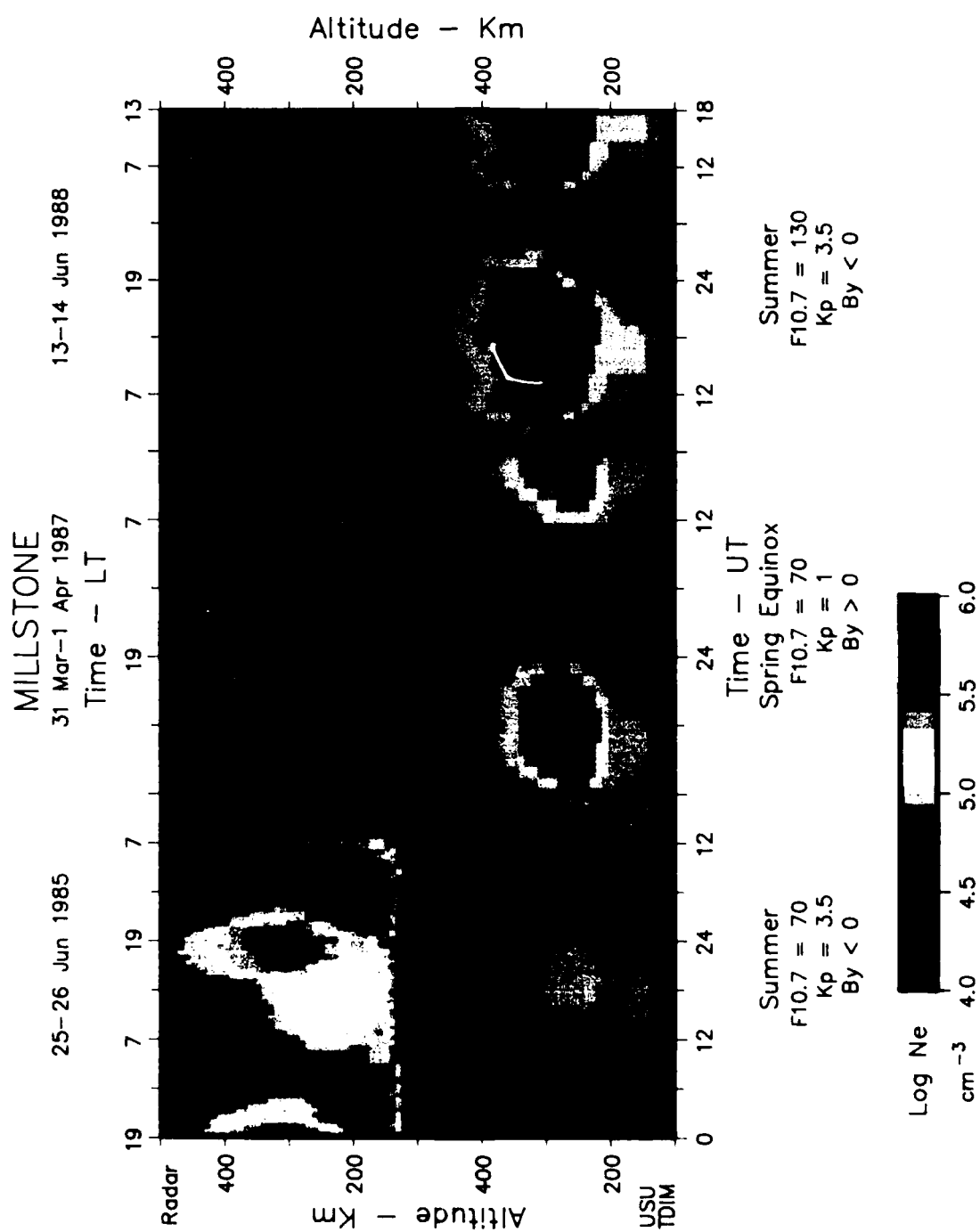




Plate 14. High-latitude winter case with geomagnetic activity #1

## SONDRESTROM

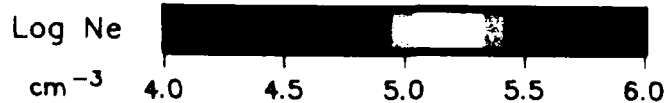
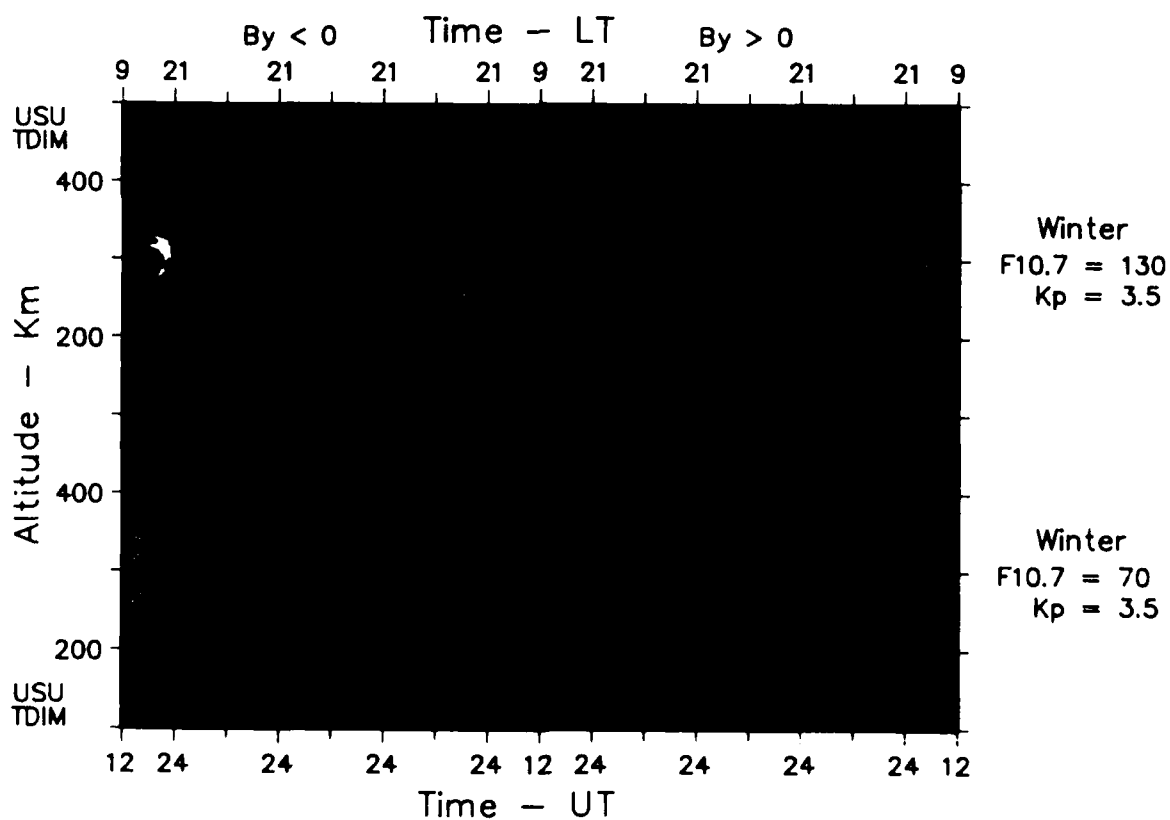
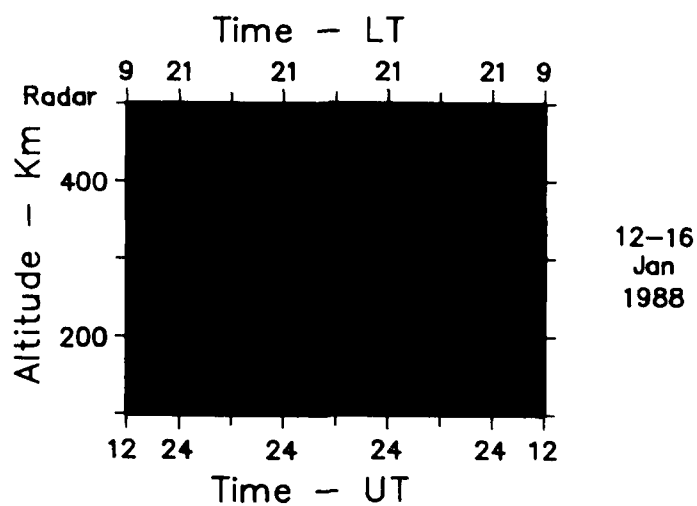
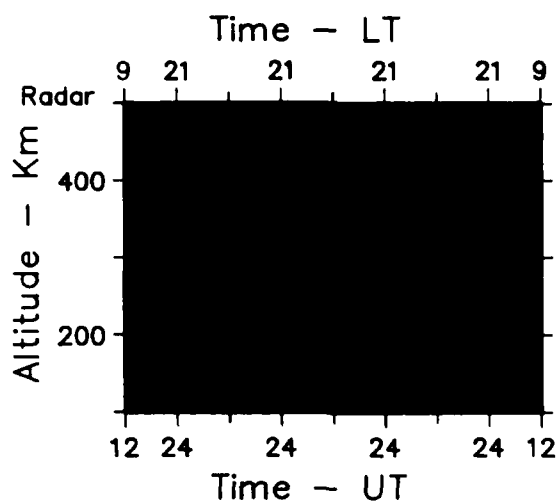
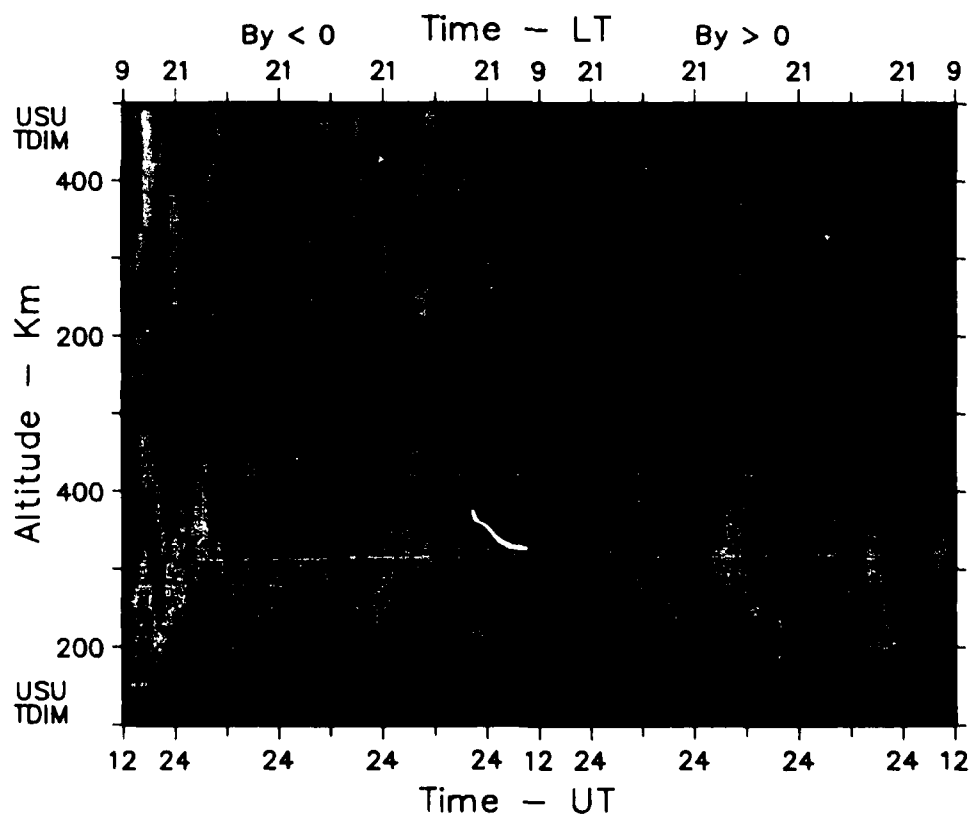


Plate 15. High-latitude winter case with geomagnetic activity #2

## SONDRESTROM



12-16  
Jan  
1988



Winter  
F10.7 = 130  
Kp = 6

Winter  
F10.7 = 70  
Kp = 6

Log Ne

cm<sup>-3</sup>

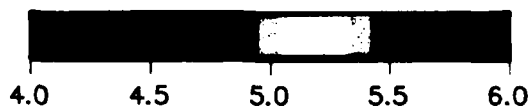
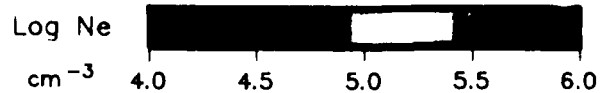
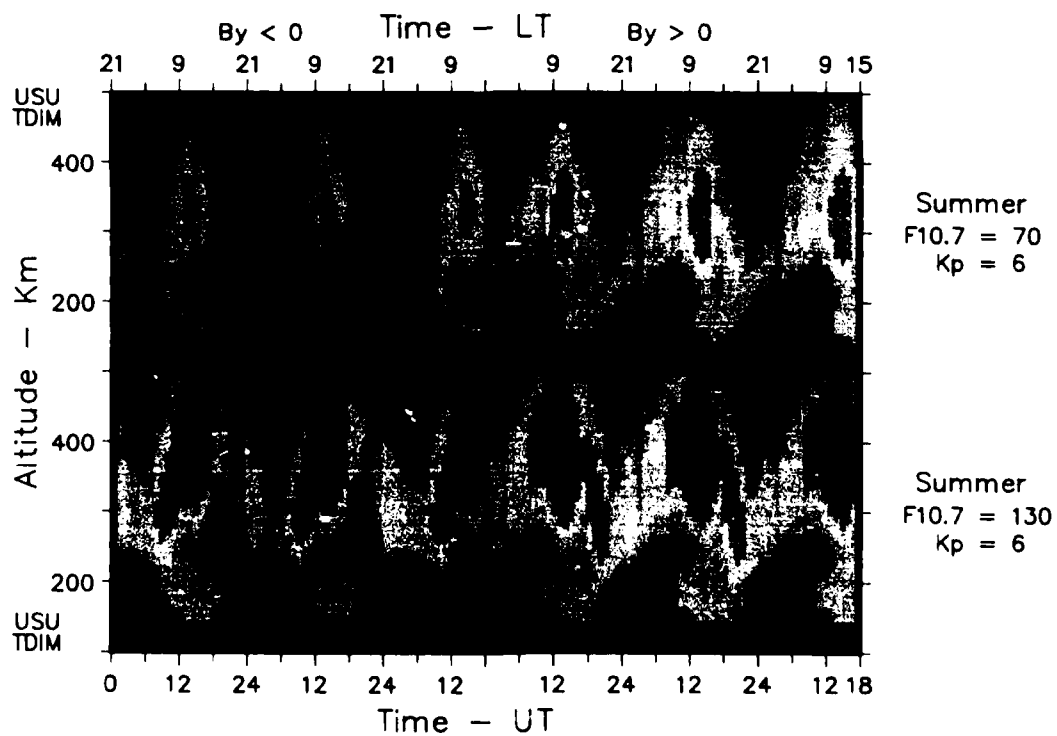
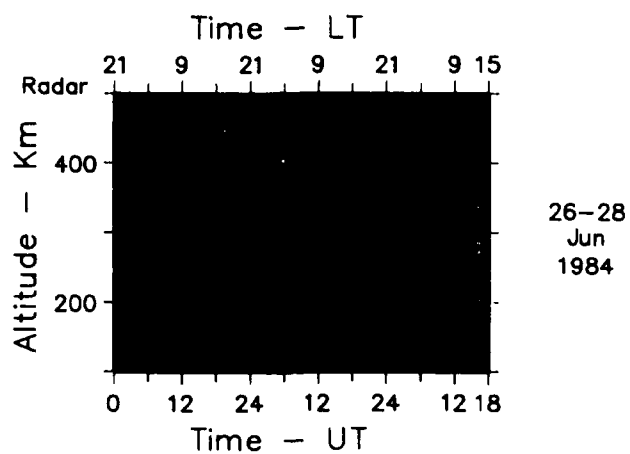


Plate 16. High-latitude summer case with geomagnetic activity

## SONDRESTROM



#### 4.14 Plate 17, Solar-Cycle Variation

The period of this study covers 3 1/2 years approximately centered about the last solar-cycle minimum in 1986. Therefore the observed solar flux represents about 1/4 of the full solar-cycle. This plate shows the effects of a varying observed average solar flux ( $\overline{Sa}$ ) for the comparison period (note that  $Sa$  and  $F10.7$  are almost equivalent solar flux parameters and can be used interchangeably as discussed in section 3.3.2). The average flux values are shown on the right-hand-side of the plate, these values ranged from near 100 at the beginning of the period, to near 70 toward at solar minimum (in 1986), and back up to near 120 towards the end of the period of study.  $Kp$  values for the 1984 and 1985 periods are relatively low;  $Kp$  for the 1988 period was relatively high and variable. See Table 4 for observed  $Sa$  and  $Kp$  values. The 1984 - 1985 comparison shows very little difference in  $HmF2$  and only slightly higher  $NmF2$  for the 1984 case. The 1985 - 1988 comparison clearly shows higher  $HmF2$  and  $NmF2$  for the 1988 case. The increased solar-flux in 1988 is likely to be the primary cause of these higher values since they are observed even at the lower latitudes where geomagnetic effects are not usually seen.

#### 4.15 Plate 18, Seasonal Variation

This plate demonstrates the seasonal variation observed at the radars and their model equivalents. The model reproduces most of the summer-winter differences including (for summer conditions): longer daytime production, generally higher  $HmF2$ 's, and for

Plate 17. Solar-cycle variation





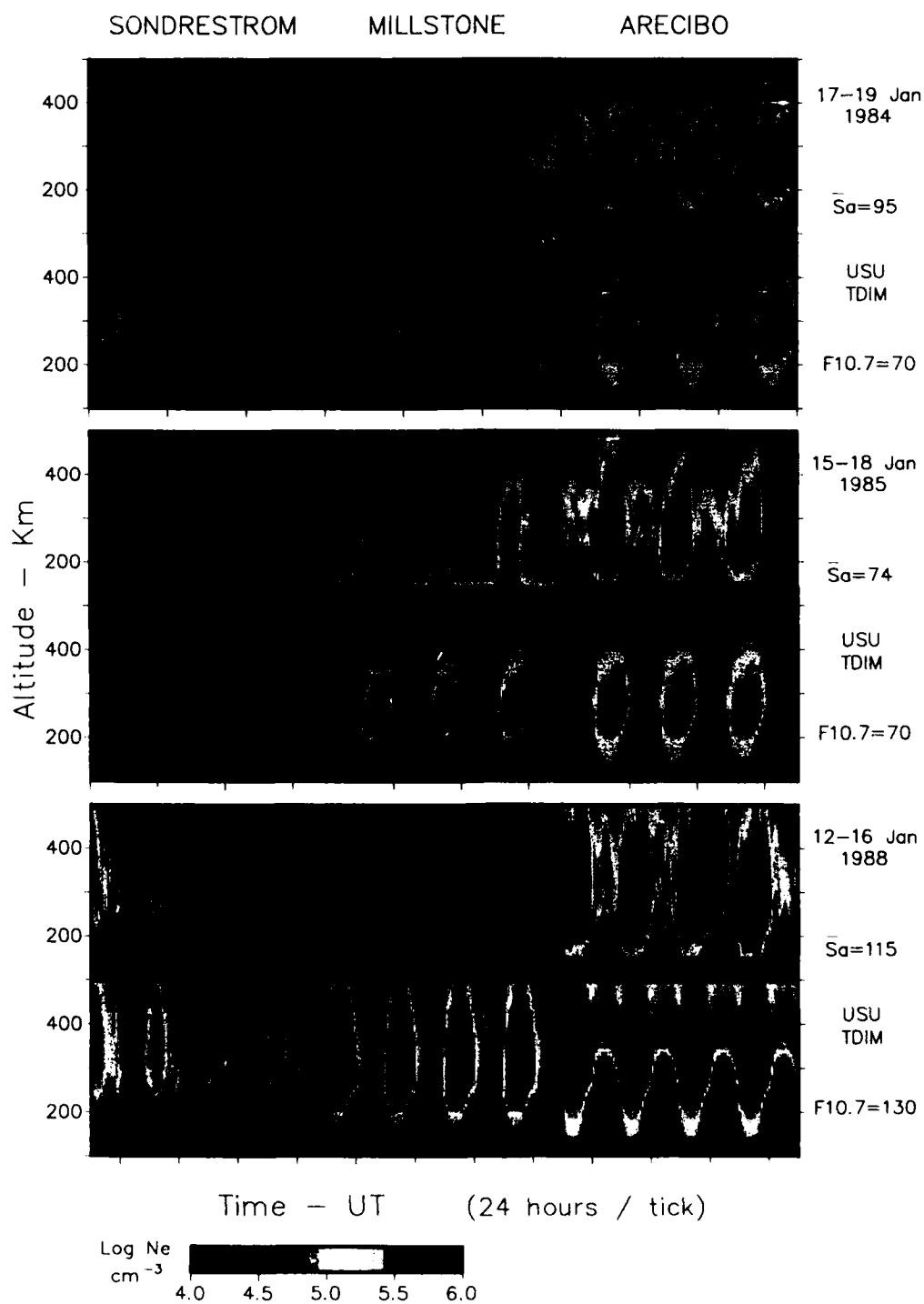
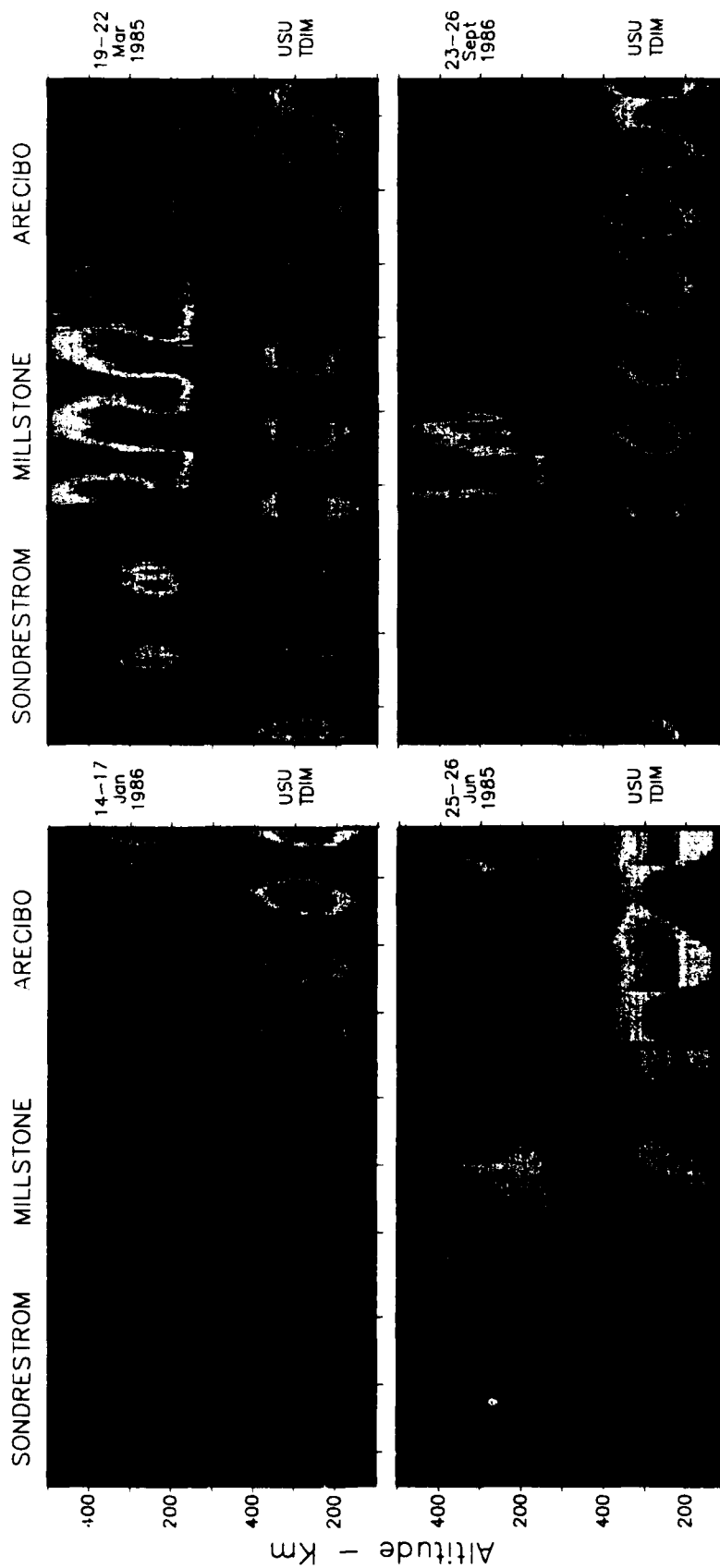


Plate 18. Seasonal variation



(24 hours / tick)



Sondrestrom and Arecibo less degradation of the nighttime F2-layer. Notice the summer period shows similar characteristics to that found for the summer period of Plate 9-- good model-reproduction at high latitudes but marginal model-reproduction of mid and low latitudes. Spring-fall equinox comparisons are very similar at Arecibo, show higher spring-equinox daytime-NmF2 at Millstone, and show significant differences (discussed in section 4.11) at Sondrestrom. These days were selected because they all were near solar-minimum conditions (with low Sa flux) and had relatively low Kp conditions. Kp for both the January and March cases were very low, while values for June and September were slightly higher. See Table 4 for observed-solar and -geomagnetic conditions.

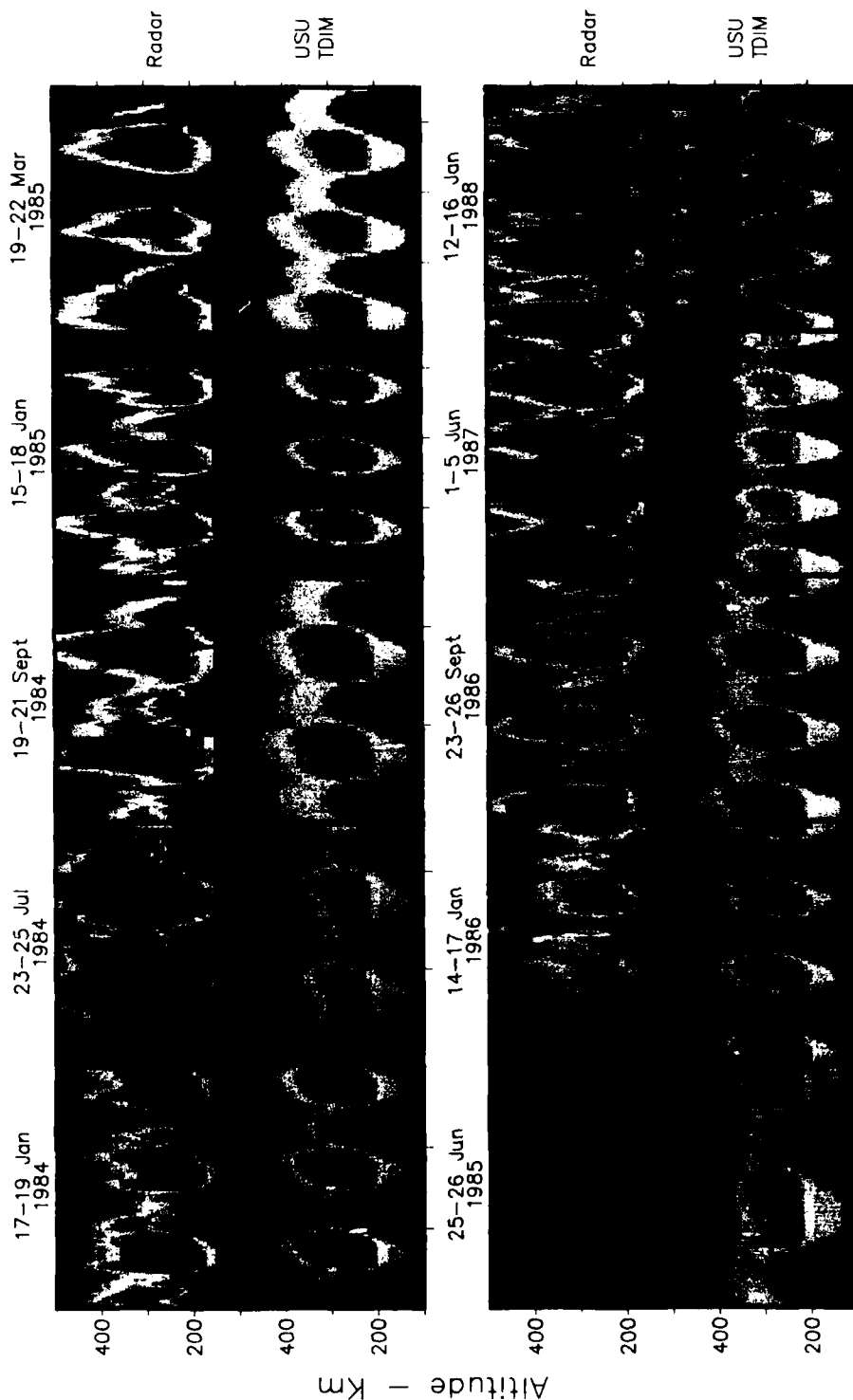
#### **4.16 Plate 19, Daytime NmF2 Differences at Arecibo**

This plate shows quite dramatically the daytime NmF2 differences between observed and modelled conditions. Two cases show relatively good agreement, 17-19 January 1984 and 12-16 January 1988. In general though, observed-daytime NmF2's were 2-4 times higher than in the model; for the worse case (1 June 1987), the observed densities were 16 times higher than in the model.

Plate 19. Daytime NmF2 differences at Arecibo



# ARECIBO



## CHAPTER V

### DISCUSSION AND CONCLUSIONS

#### 5.1 Summary of Major Trends Found

There are five major trends clearly evident from the data analysis. They are

1. On average, there is very good agreement between observed and model densities.
2. The model does not reproduce a secondary evening peak at Millstone.
3. Fall-equinox observations at Sondrestrom are not well reproduced using a spring-equinox model-day.
4. Tidal effects at Arecibo are not reproduced by the model.
5. Peak-daytime NmF2's at Arecibo do not agree.

These findings are significant because this study includes over 50 individual days; encompasses different seasons, Sa, and Kp over 3 1/2 years; and uses three radars in very different geomagnetic regions.

In order to be objective about the comparison, I grouped ionospheric features into those of primary and secondary importance when analyzing the data. This allowed me to separate major similarities and differences from those of less importance. The primary features compared were peak density found in an altitude profile (NmF2), the height of that peak density (HmF2), and the time variation of NmF2 and HmF2. In addition, color plates allowed me to easily distinguish secondary features such as structure, perturbations

in the time variation of NmF2 and HmF2, asymmetries in the daytime peaks, density differences at the top and bottom of the layer, and so on. A discussion of the major trends follows.

#### *5.1.1 Overall Agreement Between the Model and Observations*

The most striking trend found, is the overall agreement between the model and the observations. Most of the primary ionospheric features were reproduced in the model for the majority of cases. In addition, a number of secondary features were reproduced. The best comparisons are those in which model inputs are best defined. For instance, comparisons at high latitude are generally better when there is little variability in the observed geomagnetic indicator (Kp). As another example, one of the best overall comparisons found in this study was for the 14-17 January 1986 case, where observed-solar and -geomagnetic parameters were constant through the period (see Table 4); additionally, these parameters were very close to the actual model inputs used. Geophysical inputs such as the neutral atmosphere, convection pattern, and particle precipitation are statistical averages. Because these geophysical inputs were held constant for the model calculations, the TDIM cannot be expected to closely reproduce observations during periods when there is a high degree of variability in the geophysical conditions.

The USU-TDIM showed a great deal of sensitivity to geomagnetic (Kp) and especially to IMF ( $B_y > 0$ ,  $B_y < 0$ ) inputs at Sondrestrom, while these inputs had little or no effect at Millstone and Arecibo. These sensitivities were reflected in the model-



radar comparisons to a remarkable extent. Plates 14-16 show quite clearly the differences in the modelled IMF for cases of  $B_y < 0$  and  $B_y > 0$ . This type of IMF effect at high latitudes has been well observed for the convection pattern [*e.g.*, *de la Beaujardiere et al.*, 1985a] and modelled in densities [*Sojka et al.*, 1983; *Rasmussen et al.*, 1986].

### 5.1.2 Secondary Evening Peak at Millstone

Another trend is the secondary evening peak in the Millstone observations that occurred in-some-degree during nearly every experiment, and was not reproduced by the model. This feature seems to be strongest during summer and weakest during winter, with equinox lying in-between. The onset time is usually near 20 UT [15 LT] and the phenomena spans 6-8 hours of local time in the summer, 4-7 hours during spring and fall equinox, and 2-4 hours in winter (when it occurs).

The secondary evening peak is not a new observation. *Evans* [1965] describes the evening peak being caused at least in part by a rapid redistribution of ionization above HmF2 caused by a rapid fall in  $T_e$  near sunset. However, this does not explain why the effect sometimes lasts 4-6 hours after sunset. *Evans* [1973] describes an early Millstone incoherent-scatter experiment which extended over several seasons during 1966-1967 and covered solar and geomagnetic conditions similar to those in this study. The observed evening Millstone densities exhibited almost identical behavior as that found for the period of this comparison, thus providing an independent confirmation of the feature. *Evans* explains that the evening peak is more pronounced due to a mid-day suppression of ionization at Millstone caused by a northward mid-day neutral-wind forcing of the F2-layer into lower regions of the ionosphere where high-recombination rates are present; I

should point out that he was making this hypothesis without being able to measure the neutral wind, as we can now. He also attributes the summertime predominance of this feature to be due in part to a neutral-composition change which enhances loss rates during the day.

The fact that the model does not reproduce densities observed in the regularly occurring secondary peak serves to highlight this anomaly and indicates a weakness in one or more of the model inputs. An examination of those inputs most likely to explain this model-radar difference follows, (the most probable causes are listed first). One possibility is that provided by Evans' explanation of the feature, and that is a difference between model-input and observed  $T_e$  near sunset. A second possibility is a difference between modelled and actual neutral winds for Millstone latitudes. A mid-day northerly-wind as suggested by Evans is not really suspect because the model reproduced those densities, however, a rapid relative-change of neutral winds in a period ranging from 20-04 UT [15-23 LT] would help explain the feature. It should be noted that a preliminary investigation of Millstone radar-derived winds does not support this hypothesis; these winds were obtained from V. B. Wickwar, personal communication, 1990, for a period coincident with this study. A third possibility is that there is a daytime-evening neutral-composition change that is not input through MSIS-86. A fourth possibility is a topside flux, possibly due to interhemispheric flow that would enhance evening densities at Millstone-- the model does not allow for these fluxes because of an assumption that they are negligibly small. A fifth possibility is a subauroral enhancement of the eastward convection-electric-field that would produce a vertical component to an  $\mathbf{E} \times \mathbf{B}$  drift,

therefore raising HmF2. A sixth possibility is transport of dayside densities across the polar cap by  $\mathbf{E} \times \mathbf{B}$  convection (a tongue of ionization) that is more latitudinally extensive than that produced by the model. High densities associated with this phenomena have been observed for example at EISCAT [*de la Beaujardiere et al.*, 1985b]. However, there are factors repudiating this hypothesis. For instance, the feature did not show an interrelation to geomagnetic activity, even though one would expect this for an  $\mathbf{E} \times \mathbf{B}$  drift where the E-field should be highly responsive to geomagnetic activity. Additionally, while the secondary peak does show a predominance for summer, it was also consistently observed at equinox, and to a lesser extent during winter. It is not likely that convection boundaries would be consistently located close enough to Millstone latitudes to cause a "tongue of ionization" for the number of cases that I observed, especially for winter and equinox conditions. Summarizing, a satisfactory explanation pinpointing a specific model-input weakness cannot immediately be provided. The answer is probably a complex combination of these features and others, which occur at Millstone between 20-04 UT [15-23 LT]. Clearly, more research needs to be done to clarify the reason for this observation-model difference.

### 5.1.3 Spring-Fall Equinox Differences

The third major trend that I identified is the inability of the model to reproduce fall equinox observations at Sondrestrom when using a spring-equinox model-day input. Whereas the spring-equinox model gives satisfactory results at Millstone and Arecibo for both equinoxes. The solution to this problem might appear to be quite simple-- run the model for fall equinox. But what would be different? For instance, the neutral wind

input to the model is identical at spring and fall equinox. In addition, solar-EUV inputs are independent of seasonal changes and do not account for this trend. Finally, neutral densities from MSIS-86 are almost identical in these two seasons. One thing is certain, an observational pattern was established in this comparison that differentiated spring and fall conditions at Sondrestrom. The reason for these differences should be examined in the future.

#### *5.1.4 Tidal Structure at Arecibo*

Another trend found in this study is the importance of tides on the electron density structure at Arecibo. Tidal structure is not included in the Arecibo model runs. Tides are coupled to the ionosphere through the neutral wind pattern: they typically exhibit diurnal, semidiurnal, and perhaps higher order periods. At Arecibo, the semidiurnal component is by far the most predominant mode, it contributes to the so called "midnight collapse" [Nelson and Cogger, 1971; Herrero and Meriwether, 1980] and provides for the structure observed in many of the "World Days" used in this study. The tidal modes have been examined by Cray and Forbes [1986]. This structure was not seen at Millstone for example because of the decrease of the semidiurnal mode in the F-region at that latitude [e.g., Salah, 1974; Fesen et al., 1986; and Forbes 1987]. These features are not included in the TDIM adopted neutral wind. In fact, there are no daytime input neutral winds at Arecibo and only a small equatorward wind at night. Clearly, a more sophisticated thermospheric wind input is needed before such features can be reproduced.

### 5.1.5 Daytime NmF2 Differences at Arecibo

The final trend found is the disagreement between modelled and observed daytime NmF2 values at Arecibo. Generally, observed values were 2-4 times higher than in the model, see section 4.16. The reason for this trend is not at all clear. The most questionable model inputs and assumptions most likely to cause a change in daytime NmF2 would actually decrease those values if the inputs were improved upon. For instance, adding a daytime northward-neutral-wind component to the model would force the F2-layer down into regions of higher recombination and decrease NmF2. Allowing for a diffusive outflow through the top-side ionosphere would also decrease NmF2. Neutral densities as input through MSIS-86 are not likely to be in error to such an extent as to cause 2-4 times differences in electron densities every day. In fact, several studies suggest that the MSIS neutral densities are very good [Cogger *et al.*, 1980; Burnside and Sulzer, 1988].

A preliminary ionosonde-radar comparison was made in conjunction with this study for one Arecibo "World Day" from 26-28 June 1984. That comparison verified the radar observations for that period.

A comparison of the USU-TDIM with Arecibo incoherent-scatter data has not been done in the past, thus this is a new result. However, Sica *et al.* [1990] performed an extensive TDIM-ionosonde NmF2-comparison involving the model and simultaneous mid-latitude ionosonde measurements acquired between September 21 and October 5, 1986, thus overlapping with the radar data acquired between September 23 and 26, 1986, shown in this study. The ionosonde data were separated into nearby locations with similar

diurnal variations of NmF2 and then grouped together by geographic latitude and longitude. Two of these groupings were for northern-hemisphere sites with average geomagnetic latitudes similar to Arecibo; the model comparisons showed good agreement of NmF2. This is in contrast to the factor 2-4 difference found for the radar-model comparison at Arecibo in this time interval. However, while the ionosonde stations used were similar to Arecibo in geomagnetic latitude, they were not at all longitudinally similar, and their geographic latitudes were about 20° higher than Arecibo's, these differences may be significant. Another TDIM-ionosonde comparison [Sojka *et al.*, 1988] was described in section 2.3. The sites involved were closer to the Arecibo longitude. Although this study again showed good agreement between model derived and ionosonde measured  $f_oF2$ , it was even more dissimilar to the current study geographically, as the ionosonde location was at 65.3°S, 64.3°W.

The TDIM-radar electron density difference found in this comparison is both large and mysterious. Before investing much effort into trying to find an explanation, it would be a good idea to compare systematically the radar densities to simultaneous co-located ionosonde observations, and to verify the Arecibo model runs. If the difference persists, it is so large that its explanation may well provide new insight.

#### 5.1.6 Other Possible Trends

Other features were observed in the comparison which occurred on certain days or seasons but could not really be established as a trend. For example, the June 1984 "World Day" exhibited high modelled HmF2 compared to the observations, as discussed in section 4.3.; however, this feature did not occur in other June periods at Sondrestrom

and therefore is not identified as a trend.

## 5.2 Conclusions

The most striking trend found in this comparison is that the model reproduced the observed densities to a level which seems to be limited only by its inputs. That is, where trend differences existed they can most likely be traced to limitations of model inputs. The only possible exception to this is the model-observed differences at Arecibo for daytime NmF2. These differences need to be verified as real before a physical reason for them is examined.

## 5.3 Recommendations for Future Study

The objective of this study was to identify the trends in an observation-model comparison. Several trends were listed at the beginning of this chapter and have been discussed. In addition, several new questions have been raised that lead to recommendations for future research.

First, daily model-input sensitivities during the 20-04 UT [15-23 LT] period at Millstone should be investigated. For instance, a comparison of modelled-input  $T_e$  and observed  $T_e$  near sunset would determine if this contributes to the lack of a secondary peak. Another possibility is a comparison of the model input neutral winds with Millstone radar derived (or Fabry-Perot measured) winds to determine this input's contribution. In addition, a comparison of MSIS-86 neutral density inputs, with (for instance) Millstone radar derived neutrals, would help to determine the role this input has

in the lack of the feature in the model. After the model inputs responsible for this trend have been identified it may be possible to adjust them so that the TDIM can reproduce this feature.

Second, running the model for the fall-equinox days used in this study would be useful in verifying that a fall-spring input distinction is important.

Third, plotting Arecibo ionosonde data for the period of this study and possibly re-checking and re-running the USU-TDIM would be useful to verify that the Arecibo NmF2 trend is real. If it is, what is the physical reason? This could be a complex problem.

Fourth, much of the observational radar data for this study had not been previously plotted. Many interesting periods were uncovered. For instance, a detailed analysis of 14 January 1988 at Millstone and Arecibo may give insight into the response of the ionosphere at lower latitudes due to a magnetic storm. As another example, a model run for 26-28 June 1984 using more closely matched F10.7 and Kp inputs should clarify if the altitude difference was a case of poorly matched inputs or if there is something more interesting happening-- such as a high latitude difference between modelled- and observed-neutral winds. Another interesting period is 1-5 June 1987, where low-geomagnetic and -solar observations make it hard to explain the high densities found at Millstone and Arecibo; a detailed study of this period would be enlightening. There are many other examples, and this study could serve a starting point for identifying those periods where a detailed analysis could prove rewarding.

Finally, due to the detail and availability of coordinated "World Day" ISR data, other long period radar-model comparisons might be useful. For example, extending this



comparison to the St. Santin and EISCAT radars, which are in a very different longitude sector, may show new trends and verify those found here. Extending the comparisons to the Jicamarca radar and using the fully global TDIM would test the low-latitude abilities of the model. The latitudinal effects found in this study could be emphasized by calculating and comparing model and radar latitudinal density gradients. Extending the comparison to the model inputs of convection, particle precipitation, meridional wind, neutral temperature, atomic oxygen, and possibly  $T_e$  and other observed values, for a variety of latitudinal and seasonal cases, would be extremely useful in determining the importance of these inputs. Other types of model calculated parameters, such as  $T_i$  and possibly  $T_e$ , could also be used in comparisons, these test other aspects of the physics and further constrain the model.

## REFERENCES

- Appelton, E. V., and M. A. F. Barnett, On some direct evidence for downward atmospheric reflection of electric rays, *Proc. Roy. Soc. (London)*, 109, 621, 1926.
- Baron, M., O. de la Beaujardiere, and B. Craig, Project 617 radar -readiness achievement program - part A - data processing and analysis, *Rep. DASA 2519-1, 01-67-C-0019*, 138 pp., Stanford Research Institute, Menlo Park, Ca., 1970.
- Bowles, K. L., Observation of vertical-incidence scatter from the ionosphere at 41 Mc/sec, *Phys. Rev. Lett*, 1, 454, 1958.
- Breit, G., and M. Tuve, A radio method of estimating the height of the conducting layer, *Nature*, 116, 357, 1925.
- Burnside, R. G., and M. P. Sulzer, Determination of thermospheric temperatures and neutral densities at Arecibo from the ion energy balance, *J. Geophys. Res.*, 93, 8642, 1988.
- Coffey, H. E., Geomagnetic and solar data, *J. Geophys. Res.*, 89, 6853, 1984.
- Cogger, L. L., J. C. G. Walker, J. W. Meriwether, R. G. Burnside, F region airglow: are ground-based observations consistent with recent satellite results?, *J. Geophys. Res.*, 85, 3013, 1980.
- Conrad, J. R., and R. W. Schunk, Diffusion and heat flow equations with allowance for large temperature differences between interacting species, *J. Geophys. Res.*, 84, 811, 1979.
- Crary, D. J., and J. F. Forbes, The dynamic ionosphere over Arecibo: a theoretical investigation, *J. Geophys. Res.*, 91, 249, 1986.
- de la Beaujardiere, O., V. B. Wickwar, J. D. Kelly, and J. H. King, Effect of the interplanetary magnetic field y-component on the high-latitude nightside convection, *J. Geophys. Res.*, 12, 461, 1985a.
- de la Beaujardiere, O., V. B. Wickwar, G. Caudal, J. M. Holt, J. D. Craven, L. A. Frank, L. H. Brace, D. S. Evans, J. D. Winningham, and R. A. Heelis, Universal time dependence of nighttime F region densities at high latitudes, *J. Geophys. Res.*, 90, 4319, 1985b.
- Dougherty, J. P., and D. T. Farley, A theory of incoherent scattering of radio waves by a plasma, *Proc. Roy. Soc. (London)*, A259, 79, 1960.

- Evans, J. V., Cause of the mid-latitude evening increase in  $f_oF_2$ , *J. Geophys. Res.*, 70, 1175, 1965.
- Evans, J. V., Theory and practice of ionosphere study by Thomson scatter radar, *Proc. IEEE*, 57, 496, 1969.
- Evans, J. V., Millstone Hill Thomson scatter results for 1966 and 1967, *Planet. Space Sci.*, 21, 763, 1973.
- Evans, J. V., High-power radar studies of the ionosphere, *Proc. IEEE*, 63, 1636, 1975.
- Evans, J. V., J. M. Holt, and R. H. Wand, Millstone Hill incoherent scatter observations of auroral convection over  $60^\circ < \Lambda < 75^\circ$ . 1. Observing and data reduction procedures, *J. Geophys. Res.*, 84, 7059, 1979.
- Feldstein, Y. I., and G. V. Starkov, Dynamics of auroral belt and polar geomagnetic disturbances, *Planet. Space Sci.*, 15, 209, 1967.
- Fesen, C. G., R. E. Dickinson, R. G. Roble, Simulation of the thermospheric tides at equinox with the National Center for Atmospheric Research thermospheric general circulation model, *J. Geophys. Res.*, 91, 4471, 1986.
- Forbes, J. M., Modelling the propagation to atmospheric tides from the lower to the middle and upper atmosphere, *Physica Scripta*, T18, 240, 1987.
- Gordon, W. E., Incoherent scattering of radio waves by free electrons with applications to space exploration by radar, *Proc. IRE*, 46, 1824, 1958.
- Hagfors, T., Density fluctuations in a plasma in a magnetic field with applications to the ionosphere, *J. Geophys. Res.*, 66, 1699, 1961.
- Hedin, A. E., MSIS-86 thermospheric model, *J. Geophys. Res.*, 92, 4649, 1987.
- Herrero, F. A., and J. W. Meriwether, 6300-Å airglow meridional intensity gradients, *J. Geophys. Res.*, 85, 4191, 1980.
- Kelly, J. D., Sondrestrom radar -- initial results, *Geophys. Res. Lett.*, 10, 1112, 1983.
- Knecht, D. J., and B. M. Shuman, The geomagnetic field, in *Handbook of Geophysics and the Space Environment*, edited by A. S. Jursa, p. 4-1, National Technical Information Center, Springfield, Va., 1985.
- Kofman, W., and V. Wickwar, Plasma line measurements at Chatanika with high-speed correlator and filter bank, *J. Geophys. Res.*, 85, 2998, 1980.

Moorcroft, D. R., On the power scattered from density fluctuations in a plasma, *J. Geophys. Res.*, 68, 1321, 1963.

Murdin, J., J. J. Sojka, and R. W. Schunk, Diurnal transport effects on the F-region plasma at Chatanika under quiet and disturbed conditions, *Planet. Space Sci.*, 32, 47, 1984.

Murphy, J. A., G. L. Bailey, and R. Moffett, Calculated daily variations of  $O^+$  and  $H^+$  at mid-latitudes, *J. Atmos. Terr. Phys.*, 38, 351, 1976.

Nagy, A. F., and R. W. Schunk, Ionosphere, in *Encyclopedia of Physical Science and Technology* (vol. 7), edited by R. A. Meyers, p. 19, Academic Press, New York, 1987.

Nelson, G. J., and L. L. Cogger, Dynamical behavior of the nighttime ionosphere at Arecibo, *J. Atmos. Terr. Phys.*, 33, 1711, 1971.

Rasmussen, C. E., R. W. Schunk, J. J. Sojka, V. B. Wickwar, O. de la Beaujardiere, J. Foster, J. Holt, D. S. Evans, and E. Nielsen, Comparison of simultaneous Chatanika and Millstone Hill observations with ionospheric model predictions, *J. Geophys. Res.*, 91, 6986, 1986.

Ratcliffe, J. A., *The Magneto-Ionic Theory and Its Application to the Ionosphere*, 254 pp. Cambridge University Press, London, 1959.

Rishbeth, H., Basic physics of the ionosphere: a tutorial review, *J. IERE*, 58, S207, 1988.

Roble, R. G., The calculated and observed diurnal variation of the ionosphere over Millstone Hill on 23-24 March 1970, *Planet. Space Sci.*, 23, 1017, 1975.

Roble, R. G., and M. H. Rees, Time-dependent studies of the aurora: Effects of particle precipitation on the dynamic morphology of ionospheric and atmospheric properties, *Planet. Space Sci.*, 25, 991, 1977.

Salah, J. E., Daily oscillations of the mid-latitude thermosphere studied by incoherent scatter at Millstone Hill, *J. Atmos. Terr. Phys.*, 36, 1891, 1974.

Salpeter, E. E., Electron density fluctuations in a plasma, *Phys. Rev.*, 120, 1528, 1960.

Schunk, R. W., Ambipolar Diffusion in the F1-region of the ionosphere, *Planet. Space Sci.*, 21, 526, 1973.

Schunk, R. W., Mathematical structure of transport equations for multispecies flow, *Rev. Geophys. Space Phys.*, 15, 429, 1977.

Schunk, R. W., The terrestrial ionosphere, in *Solar Terrestrial Phys*, edited by R. L. Corovillano and J. M. Forbes, pp. 609, D. Reidel, Dordrecht, 1983.

Schunk, R. W., A mathematical model of the middle and high latitude ionosphere, *PAGEOPH (Switzerland)*, 127, 255, 1988.

Schunk, R. W., and W. J. Raitt, Atomic nitrogen and oxygen ions in the daytime high-latitude F-region, *J. Geophys. Res.*, 85, 1255, 1980.

Sica, R. J., R. W. Schunk, and P. J. Wilkinson, A study of the undisturbed mid-latitude ionosphere using simultaneous multiple site ionosonde measurements during the Sundial-86 campaign, *submitted to J. Geophys. Res.*, 1990.

Sojka, J. J., Global scale, physical models of the F-region ionosphere: a review, *Rev. Geophys.*, 27, 371, 1989.

Sojka, J. J., R. W. Schunk, J. V. Evans, J. M. Holt, and R. H. Wand, Comparison of model high-latitude electron densities with Millstone Hill observations, *J. Geophys. Res.*, 88, 7783, 1983.

Sojka, J. J., C. E. Rasmussen, and R. W. Schunk, An interplanetary magnetic field dependent model of the ionospheric convection electric field, *J. Geophys. Res.*, 91, 11281, 1986.

Sojka, J. J., R. W. Schunk, and G. L. Wrenn, A comparison of  $f_oF_2$  obtained from a time-dependent ionospheric model with Argentine Islands data for quiet conditions, *J. Atmos. Terr. Phys.*, 50, 1027, 1988.

St-Maurice, J-P, J. C. Foster, J. M. Holt, and C. del Pozo, First results on the observation of 440-MHz high-latitude coherent echoes from the E region with the Millstone Hill Radar, *J. Geophys. Res.*, 94, 6771, 1989.

Sulzer, M. P., A phase modulation technique for a sevenfold statistical improvement in incoherent scatter data-taking, *Radio Sci.*, 21, 737, 1986.

Torr, M. R., D. G. Torr, R. A. Ong, and H. E. Hinteregger, Ionization frequencies for major thermospheric constituents as a function of solar cycle 21, *Geophys. Res. Lett.*, 10, 771, 1979.

Wickwar, V. B., Analysis techniques for incoherent-scatter data interpretation in the 100-to-300-km region, *Rep. DNA-3335T, 001-72-C-0076*, 86 pp., Stanford Research Institute, Menlo Park, Ca., 1974.

Wickwar, V. B., J. D. Kelly, O. de la Beaujardiere, C. A. Leger, F. Steenstrup, and C. H. Dawson, Sondrestrom overview, *Geophys. Res. Lett.*, 1, 883, 1984.

Wilkinson, P. J., R. W. Schunk, R. Hanbaba, and H. Mori, Interhemispheric comparison of SUNDIAL F-region data with global scale ionospheric models, *Ann. Geophys.*, 6, 31, 1987.

Wrenn, G. L., A. S. Rodger, and H. Rishbeth, Geomagnetic storms in the Antarctic F-region. I. Diurnal and seasonal patterns for main phase effects, *J. Atmos. Terr. Phys.*, 49, 901, 1987.

Yngvesson, K. O., and F. W. Perkins, Radar thomson scatter studies of photoelectrons in the ionosphere and Landau damping, *J. Geophys. Res.*, 73, 97, 1968.